J. Fluid Mech. (2016), *vol.* 800, *pp.* 5–56. © Cambridge University Press 2016
doi:10.1017/jfm.2016.373

Ventilated cavities on a surface-piercing hydrofoil at moderate Froude numbers: cavity formation, elimination and stability

Casey M. Harwood[1,†], Yin L. Young[1] and Steven L. Ceccio[1,2]

[1]Department of Naval Architecture and Marine Engineering, University of Michigan, Ann Arbor, MI 48109, USA

[2]Department of Mechanical Engineering, University of Michigan, Ann Arbor, MI 48109, USA

(Received 29 May 2015; revised 1 May 2016; accepted 29 May 2016; first published online 29 June 2016)

The atmospheric ventilation of a surface-piercing hydrofoil is examined in a series of towing-tank experiments, performed on a vertically cantilevered hydrofoil with an immersed free tip. The results of the experiments expand upon previous studies by contributing towards a comprehensive understanding of the topology, formation and elimination of ventilated flows at low-to-moderate Froude and Reynolds numbers. Fully wetted, fully ventilated and partially ventilated flow regimes are identified, and their stability regions are presented in parametric space. The stability of partially and fully ventilated regimes is related to the angle of the re-entrant jet, leading to a set of criteria for identifying flow regimes in a laboratory environment. The stability region of fully wetted flow overlaps those of partially and fully ventilated flows, forming bi-stable regions where hysteresis occurs. Ventilation transition mechanisms are classified as formation and elimination mechanisms, which separate the three steady flow regimes from one another. Ventilation formation requires air ingress into separated flow at sub-atmospheric pressure from a continuously available air source. Ventilation washout is caused by upstream flow of the re-entrant jet. The boundary denoting washout of fully ventilated flow is expressed as a semi-theoretical scaling relation, which captures past and present experimental data well across a wide range of Froude and Reynolds numbers.

Key words: cavitation, gas/liquid flow, multiphase flow

1. Introduction

Ventilation occurs when air or other non-condensible gas is entrained in a hydraulic flow, often from a free surface. Many high-lift devices, such as propellers and hydrofoils, that operate near or at a free surface are prone to atmospheric ventilation. Ventilated flows can be leveraged to improve the stability and efficiency of lift-generating devices operating at specific conditions; examples include air injection on supercavitating propellers and parasitic drag reduction in surface-piercing propellers. Conversely, when unwanted ventilation occurs, the transition from low-pressure wetted

† Email address for correspondence: cmharwoo@umich.edu

flow to relatively high-pressure aerated flow can cause dramatic reductions in lift and efficiency. Stepped bottoms and hard chines on planing-craft hulls, the sharp demi-hulls of multi-hulled vessels, and waterjet inlets are other examples of entities subjected to atmospheric ventilation.

In this work, the atmospheric ventilation of a surface-piercing hydrofoil is investigated at low-to-moderate Froude numbers, with a focus on the formation, elimination and stability of ventilated cavities. In performing this work, the authors strive to expand upon the body of existing research, and to elucidate upon some previously disparate concepts in the comprehension of atmospheric ventilation. The work addresses this overarching objective in the following ways. (1) Characteristic steady flow regimes are formally classified, and the stability and hydrodynamic performance of the hydrofoil in each flow regime are quantified. (2) The transition mechanisms of ventilation formation and elimination are formally classified, and the flow conditions permitting ventilation formation and/or elimination are identified. (3) A scaling relationship is developed for the stage of ventilation elimination known as 'washout'.

Section 1.1 contains a survey of the literature. In § 1.2, a modified lifting-line model is briefly described, which is used to complement the experimental results and provide insight into the physics of ventilated cavity flow. The experimental programme is described in § 2. Steady flow regimes are discussed in § 3, with a discussion of the re-entrant jet in § 3.1, a strengthened set of classification criteria in § 3.2, a discussion of steady hydrodynamic loading in § 3.3 and a parametric representation of flow-regime stability boundaries in § 3.4. In § 4, the unsteady transition processes that move the flow between stable regimes of ventilation are described, with ventilation formation mechanisms in § 4.1 and ventilation elimination mechanisms in § 4.2. To be succinct, most of the results shown are for a partial immersion depth equal to one chord length, although results from other immersion depths are used to validate the scaling approach derived in § 4.2.1. Results for all three depths of immersion may be found in appendix A. Concluding remarks are offered in § 5.

1.1. *Previous research*

Ventilated flows around surface-piercing bodies were extensively studied in the 1950s, the 1960s and the 1970s, spurred by interest in high-speed hydrofoil-supported vessels. A summary of past experimental studies is tabulated in table 1 as a convenient reference for the parameter ranges examined in each study.

Perry (1955) found that the separated wake behind bluff bodies piercing the free surface was easily aerated, and that, given a suitable perturbation, a ventilated cavity could extend beyond the low-energy wake to envelop much of the body. Kiceniuk (1954) showed that ventilation could also occur on streamlined hydrofoils when the yaw angle (α, which is also the angle of attack for vertically oriented hydrofoils and struts) exceeded the stall angle. Once a cavity was present, it remained stable across a wide range of angles, including those below the stall angle at which ventilation occurred. In both studies, air was initially entrained into low-pressure regions of separated flow, but with sufficiently large amounts of ventilation, a new stable state was reached, with a cavity extending beyond the original wetted zone of flow separation.

Wetzel (1957) performed experiments on partially immersed cylindrical rods with diameters between 0.8 mm and 5.1 cm (1/32–2 in.) and vertical symmetric struts to

https://doi.org/10.1017/jfm.2016.373 Published online by Cambridge University Press

Researchers	Geometry	c (d) (cm)	AR_h	Fn_h	$Re_c \times 10^{-5}$	$We \times 10^{-4}$	σ_v
Coffee & McKann (1953)	NACA 66_1012	10–20	1–6	2.6–24.4	9.3–49.5	11.7–166	0.3–2.6
	NACA 66_4021	10.2	1–6	3.7–24.4	9.3–24.8	11.7–83	0.3–2.5
Perry (1955)	Rect. bars	2.5	1.2–17	0.7–15.1	0.4–2.1	0.1–2.4	2.9–88
Wetzel (1957)	Circ. cyl.	0.1–5.1	1–100	0.1–65.3	0–3.1	0–5.3	5.3–353
	NACA 0012	5.1–7.6	0.5–5	0.5–12.2	0.5–4.6	0.1–8	5.3–246
	NACA 0024	5.1	0.5–4.5	0.6–12.2	0.5–3.1	0.1–5.3	5.3–242
Wadlin (1958)	NACA 64 series	—	—	—	—	—	—
Breslin & Skalak (1959)	NACA 4412	7.6	0.5–2	0.8–9.1	0.9–10.6	0.6–15	2.4–342
	Circular arc	6.4	0.5–2	0.7–16.4	0.5–5.8	0.1–7.3	2.3–343
Rothblum, Mayer & Wilburn (1969)	Biogive family	30.5	1–3	0.7–16.3	6.3–86.2	1.8–335	0.25–51
Waid (1968)	Biogive family	30.5	1–1.5	2.9–5.3	18.6–28	15.6–35	0.16–5.5
Swales *et al.* (1973)	Biogive	10.2	2	1.1–4.3	1.7–6.7	0.3–5.2	5.4–86
Swales *et al.* (1974)	Biogive	10.2	2	1.1–4.3	1.7–6.7	0.3–5.2	0.2–88
	NACA 0012	10.2	2	1.1–4.3	1.7–6.7	0.3–5.2	0.2–88
	NACA 16-021	10.2	2	1.1–4.3	1.7–6.7	0.3–5.2	0.2–88
	Biogive family	30.5	2	0.8–10.3	5.8–76.8	1.5–266	0.3–58

TABLE 1. Summary of previous studies. Included are the geometric configuration of the model, the chord length c (but in the cases where the geometry is a circular cylinder, the rod diameter d is used), the range of immersed aspect ratios $AR_h = h/c$, the range of depth Froude numbers $Fn_h = u/\sqrt{gh}$, the range of chord-based Reynolds numbers $Re_c = uc/\nu$, the range of Weber numbers $We = \rho u^2 c/\gamma$ and the range of vaporous cavitation numbers at the free-surface plane $\sigma_v = (P_atm - P_v)/(\rho u^2/2)$. Parameters not given in the original report have been calculated from the bounding values reported for test conditions. Where minimum or maximum parameter values were not stated, they were inferred from the results in the respective reports. Empty cells indicate that insufficient data about the study were provided to make an estimation.

study the scale effects associated with the transition between wetted and ventilated flows. The Reynolds number and Weber number were varied independently from the Froude number by heating the water and adding detergents respectively. While not directly reported, his data showed that the effect of Weber number was negligible above a critical value of $We = \rho u^2 l/\gamma \approx 250$, where u is the forward speed of the hydrofoil, l is the characteristic length (rod diameter d or strut section chord length c), ρ is the liquid density and γ is the surface tension constant in Nm^{-1}. In the case of yawed struts, ventilation at yaw angles of $\alpha \leqslant 21^\circ$ was hysteretic and dependent upon the yaw angle, sometimes occurring suddenly in what the author dubbed 'flash' ventilation. At angles of attack exceeding the stall angle ($\alpha \geqslant 21^\circ$), ventilation occurred gradually through entrainment of air into the stalled wake (dubbed 'creeping' ventilation). The latter type of ventilation was found to scale with the depth-based Froude number,

$$Fn_h = \frac{u}{\sqrt{gh}}, \tag{1.1}$$

where h is the static immersion depth of a surface-piercing body and g is gravitational acceleration. Large-diameter cylinders for which $We \geqslant 250$ and hydrofoils at yaw angles of $\alpha \geqslant 21^\circ$ both ventilated via the 'creeping' process at a constant $Fn_h \approx 1.7$.

Wadlin (1958) studied an unyawed vertical surface-piercing hydrofoil with a cambered section profile. Oil-smear visualizations on the suction surface indicated a laminar separation bubble near the trailing edge, but the separated flow did not extend to the free surface. When air was artificially injected into the separated flow, it displaced the water to form a cavity of approximately the same size as the preceding separation zone. Wadlin (1958) concluded that both low pressures and separated flow are required for ventilation to occur. He referenced the experiment by Coffee & McKann (1953), in which vaporous cavitation (when the liquid changes phase to vapour, caused by a reduction of the local pressure to the saturated vapour pressure of the fluid) occurred on the afterbody of an unyawed surface-piercing hydrofoil at speeds in excess of 23 m s^{-1} ($Fn_h > 16$). The presence of vaporous cavitation provided visual evidence of the necessary low pressures and flow separation, but ventilation did not automatically occur. In Wadlin's experiment, ventilation was induced by 'disturbing the water surface in the vicinity of the leading edge'. The 'disturbance' was probably a thin wire inserted into the flow, although the exact method was unspecified. The disturbance served to rupture the barrier of unseparated flow near the free surface, allowing air to enter and occupy the ventilation-ready flow. The ventilated cavity gradually disappeared once the disturbance was removed, leading Wadlin (1958) to conclude two things: first, that low-pressure paths (such as shear flows or the cores of shed vortices) must be available to permit the ingress of air into a ventilation-ready flow before ventilation can occur, and, second, that those air paths must remain available for ventilated cavities to persist.

Breslin & Skalak (1959) performed a series of experiments on yawed surface-piercing hydrofoils with and without cambered sections with chord lengths of $c = 7.6$ cm and $c = 6.4$ cm respectively. They defined ventilation as a flow regime characterized by the entrainment of a 'smooth-walled' air-filled cavity along the entire immersed span of a hydrofoil. Ventilation caused a reduction of up to 70 % in the measured lift coefficient C_L relative to fully wetted flows at the same conditions (the expression for C_L is given in § 3.3). The appearance and disappearance of ventilated cavities were respectively termed ventilation 'inception' and 'closure'. It should be noted that, in the present work, the term 'formation' is used in place of 'inception', which will be given a more specific definition in the following sections.

Likewise, 'closure' is replaced by 'elimination' to avoid confusion with the downstream extent of a gaseous cavity, known as a cavity 'closure region'. At post-stall angles of attack/yaw angles ($\alpha \geqslant 20°$), ventilation formation occurred spontaneously and gradually, with air entrainment occurring through eddies in the separated wake, similar to the base flow behind bluff bodies and highly yawed hydrofoils observed by Wetzel (1957). At angles approaching stall ($\alpha \approx 15°$–$18°$), vortices were shed by the imminently stalled flow. The shed vorticity intersected the free surface, aerating through the vortex cores and drawing air into locations of peak suction pressure on the hydrofoil to cause ventilation. At very small immersion depths and moderate angles of attack ($14° \leqslant \alpha \leqslant 18°$ and $AR_h = h/c = 0.5$, where AR_h is known as the immersed aspect ratio), ventilation formation occurred through the ingestion of air into the tip vortex far downstream of the hydrofoil, at which point the vortex core aerated, transporting air upstream to the suction side of the hydrofoil. Breslin & Skalak (1959) also showed that ventilation could be triggered at sub-stalled angles ($\alpha \leqslant 14°$) by breaching the free surface upstream of the leading edge of the hydrofoil with a disturbing body (such as the point of a pencil). Unlike Wadlin (1958), who observed ventilated cavities triggered in this manner to disappear after the disturbance was removed, Breslin & Skalak (1959) found that such cavities remained stable, even as the yaw angle was decreased towards zero degrees, corroborating the observations of Kiceniuk (1954) and Wetzel (1957). Breslin & Skalak (1959) also used oil-film visualization to demonstrate that boundary layer separation did not extend to the free surface for yaw angles below stall. Breslin & Skalak (1959) studied the conditions at cavity elimination with varying hydrofoil sections and immersed aspect ratios by decreasing the speed of a fully ventilated hydrofoil and recording C_{L_w} and Fn_h immediately following the elimination of the fully ventilated cavity, where C_{L_w} denotes the 3D lift coefficient of the fully wetted hydrofoil at the conditions under which ventilation ceased to occur (discussed further in § 4.2.1). When C_{L_w} was plotted against Fn_h^{-2}, a number of boundaries were revealed for the different foil shapes and configurations. At the limit of small Fn_h^{-2} (large Fn_h) and small C_{L_w}, the boundaries faired into a line, suggesting that fully ventilated flows were stable only if

$$C_{L_w} \geqslant 5Fn_h^{-2} \quad \text{and} \quad Fn_h \geqslant 3. \tag{1.2a,b}$$

It should be noted that, at smaller Fn_h or larger C_{L_w}, the boundaries found by Breslin & Skalak (1959) deviated from the asymptotic fit and from one another, so (1.2) overpredicted the required lift coefficient at a given Fn_h and overpredicted the Fn_h for a given lift coefficient at which stable ventilation occurred.

Rothblum *et al.* (1969) performed a series of experiments at high speeds and Reynolds numbers ($5 \times 10^5 \leqslant Re_c \leqslant 1.7 \times 10^7$) on a family of symmetric biogive-section hydrofoils with chord lengths of 0.3–0.61 m, varying leading edge radii and zero trailing edge thickness at varying yaw angles. Here, the Reynolds number is based on the chord length, or $Re_c = uc/\nu$, where ν is the fluid kinematic viscosity. He identified wetted and ventilated flow regimes, and noted the propensity of ventilated flow to remain stable at yaw angles much smaller than the conditions at formation. At speeds high enough to induce vaporous cavitation, ventilation occurred when the layer of liquid separating the vaporous cavity from the free surface was ruptured. The formation of a ventilated cavity occurred very suddenly, reducing or even reversing the action of lift. Rothblum *et al.* (1969) suggested that at moderate angles of attack, flow over the suction surface of the hydrofoil induced a downward acceleration of the free surface, creating Taylor instabilities on the free surface (Taylor 1950; Emmons, Chang & Watson 1960). Air then entered ventilation-prone zones on the suction

surface through low-pressure vortical paths created by the collapse of the Taylor instabilities. The family of biogival struts with a chord length of $c = 0.3$ m was also tested by Waid (1968) in a depressurized towing tank to study the interactions of ventilated and vaporous cavities. Cavitation numbers as low as $\sigma_v = 0.162$ were tested. Here, $\sigma_v = (P_{atm} - P_v)/(\rho u^2/2)$ is the vaporous cavitation number, where P_{atm} is the ambient pressure at the free surface and P_v is the saturated vapour pressure of freshwater. The results suggested that the value of σ_v was a primary factor governing ventilation formation when vaporous cavities were present. Taylor instabilities in the thin layer of water between a vaporous cavity and the free surface were a primary mechanism of air ingress into the low-pressure vaporous cavity.

Swales *et al.* (1973) used pressure taps and oil-film visualization on the suction surface of a yawed vertical hydrofoil with a 0.1 m chord biogival section to show that sub-atmospheric pressures and flow separation preceded ventilation formation in all cases, consistent with previous studies. The oil film indicated a long leading edge separation bubble on the suction surface, which, like those observed by Wadlin (1958) and Breslin & Skalak (1959), did not extend to the free surface at sub-stall yaw angles. This indicated that a thin layer of fluid near the free surface presented a barrier to the ingress of air. The researchers corroborated the claim of Wadlin (1958) that sub-atmospheric pressures and boundary layer separation are necessary pre-conditions of ventilation. However, they found no explicit relationship between spontaneous ventilation formation and the satisfaction of these pre-conditions, i.e. they were unable to show that the pre-conditions were sufficient to guarantee ventilation formation.

Swales *et al.* (1974) studied the same biogival model families as Rothblum *et al.* (1969) and Swales *et al.* (1973). In addition, struts with NACA-0012 and NACA-16-021 sections and 10 cm chords were used. They found that the Taylor instabilities described by Rothblum *et al.* (1969) induced ventilation formation for streamlined sections (termed 'tail inception'), while sharp-nosed sections ventilated through a long leading edge bubble and the associated leading edge vortex (termed 'nose inception'). It should be noted again that the term 'inception' describes processes that are, in this work, classified as ventilation 'formation', while 'inception' will be defined more formally in § 4.1. Leading edge separation with subsequent reattachment of the flow is a feature of sharp-nosed sections known as 'thin-airfoil stall' (Gault 1957), which occurs when adverse pressure gradients induce laminar separation upstream of the turbulent transition point. Chang (1960, 1961) states that the laminar separation point is independent of the free-stream Reynolds number on such section shapes. Hecker & Ober (1974) found that the length of separation bubbles on sharp-nosed hydrofoil sections grew as the angle of attack was increased, and depended only weakly on the Reynolds number in the range of $1 \times 10^5 \leqslant Re_c \leqslant 3 \times 10^5$. Air injected into a separation bubble by Hecker & Ober (1974) was entrained in the separated flow and formed a partial ventilated cavity, while air injected outside of the bubble was convected downstream without inducing ventilation.

Rothblum, McGregor & Swales (1974) studied the effects of surface roughness, surface wettability and speed on the formation of ventilated cavities using a strut with a 10 cm chord and NACA-0012 section profile with different surface coatings and finishes. They determined that roughened surfaces and higher speeds acted to weaken the sealing effect of the unseparated flow at the free surface by promoting turbulence and generating vorticity near the free surface. Surface wettability and surface tension were judged to have negligible influence at the scale tested.

Interested readers may find additional background in the work of Acosta (1973) and Rothblum (1977). One recurring conclusion from the studies is that ventilation

must be preceded by both sub-atmospheric pressures and boundary layer separation. Another recurring observation is that there exists an unseparated layer of flow near the free surface at angles of attack below stall. The free surface relieves chordwise pressure gradients on the hydrofoil, precluding flow separation. As a result, a thin layer of high-energy flow forms a seal between the ventilation-prone regions and the source of air, delaying ventilation, even beyond the point at which the flow could begin to sustain a ventilated cavity. This conclusion was supported by the observations of Wadlin (1958), Breslin & Skalak (1959), Rothblum *et al.* (1969) and Swales *et al.* (1974) that in some trials, sub-atmospheric pressures and separated flow were evident (inferred from pressure surveys and oil films, or indicated by the presence of vaporous cavities), even while the flow remained fully wetted. Likewise, the lack of sufficiency of sub-atmospheric separated flow for predicting ventilation formation (Swales *et al.* 1973) was thought to be a result of the free-surface seal created by the unseparated layer of flow.

Depth-based Froude numbers in the range of $1 \leqslant Fn_h \leqslant 25$ were reported for studies of streamlined struts/hydrofoils, but discussions of cavity topologies and stability were focused primarily on relatively large Froude numbers ($Fn_h \geqslant 4$), by testing at high speeds or by using very small models. In this range of Fn_h, the flows tend to be unambiguously wetted or ventilated. The transitional flows that precede fully developed ventilation, especially at lower speeds, have been largely neglected. The range of low-to-moderate Froude numbers ($0.5 \lesssim Fn_h \lesssim 4$) is an important one, however. As shown by the results of Wetzel (1957) and Breslin & Skalak (1959), ventilation formation and elimination may occur at low Froude numbers, incurring sudden changes in loading and flow topology. Additionally, while a limited number of studies have investigated ventilation formation, the process of ventilation elimination has not been examined closely, with the exception of a brief treatment by Breslin & Skalak (1959). From a design standpoint, any system designed to operate at high Froude numbers must necessarily transit the low-to-moderate Froude number range. From a scientific standpoint, it is desirable to better understand ventilation in this range of Froude numbers, where hydrostatic and dynamic pressures are of the same order of magnitude. Therefore, a more thorough investigation of flow stability and ventilation transition processes is of both practical and academic interest.

1.2. *Example cavity flow and lifting-line model*

In this section, an example of a 3D ventilated cavity will be presented to illustrate the disparity between two-dimensional (2D) and three-dimensional (3D) flow descriptors. Additionally, a simple lifting-line method is used to model the effects of dominant physics acting on a surface-piercing strut in ventilated flow.

1.2.1. *Two-dimensional cavity flows*

Two-dimensional cavity flows are characterized by the ratio of the cavity length to the chord length (L_c/c). Such cavities, whether vaporous or ventilated, are scaled with the section angle of attack (α_{2D}) and the sectional cavitation number,

$$\sigma_c = \frac{P_\infty - P_c}{1/2\rho u^2}. \tag{1.3}$$

Here, σ_c should not be confused with the vaporous cavitation number defined earlier, σ_v. The sectional cavitation number σ_c is a generalized form of the cavitation number (also known as the cavity under-pressure coefficient), where P_∞ and P_c are respectively the absolute pressure of the incoming flow and the pressure inside the

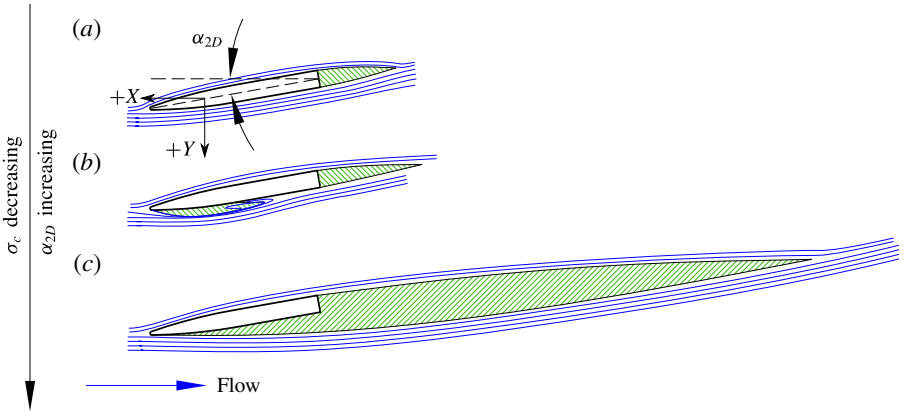

FIGURE 1. (Colour online) Two-dimensional cavity regimes on a hydrofoil section. The hydrofoil section is indicated by a black outline, cavities are indicated by green hatching and streamlines are indicated by blue lines. (*a*) Fully wetted flow lacks any attached cavity along the suction surface, but may exhibit a base cavity in the wake of a bluff body. (*b*) Partial cavitation is characterized by a cavity that does not reach the foil trailing edge. (*c*) Full/supercavitation is characterized by a cavity that extends to or beyond the foil trailing edge.

cavity, each at some depth below the free surface. Figure 1 illustrates fully wetted, partially cavitating and fully/supercavitating 2D cavity regimes and their dependence upon σ_c and α_{2D}.

The lift coefficient of a 2D section is approximated in thin-airfoil theory as

$$C_{l_{2D}} = a_0 \sin(\alpha_{2D}), \tag{1.4}$$

where a_0 (commonly referred to as the lift slope) is the tangent slope of the lift coefficient curve at small angles ($a_0 \approx \partial C_{l_{2D}}/\partial \alpha_{2D}$). Sectional lift is strongly influenced by cavitation. To model this effect, classical linear solutions for vaporous cavitating flow around a flat plate are used. For a supercavitating flat plate, Tulin (1953) gave

$$\frac{L_c}{c} = \left(\frac{2\alpha_{2D}}{\sigma_c} + \alpha_{2D}\right)^2 + 1 \approx \left(\frac{2\alpha_{2D}}{\sigma_c}\right)^2 + 1, \tag{1.5a}$$

$$a_0 = \pi \frac{L_c}{c}\left[\frac{\sqrt{L_c/c}}{\sqrt{L_c/c - 1}} - 1\right], \quad \frac{L_c}{c} > 1. \tag{1.5b}$$

Acosta (1955) gave the solution for partial cavitation on a flat plate as

$$\frac{\sigma_c}{2\alpha_{2D}} = \frac{2 - L_c/c + 2\sqrt{1 - L_c/c}}{\sqrt{L_c/c(1 - L_c/c)}}, \tag{1.6a}$$

$$a_0 = \pi\left(1 + \frac{1}{\sqrt{1 - L_c/c}}\right), \quad \frac{L_c}{c} \leqslant 0.5. \tag{1.6b}$$

The derivations of these linear solutions make no assumptions regarding the composition of gas inside the cavities, so both are judged to be applicable to ventilated cavities as long as the correct cavity pressure is used in (1.3) to compute σ_c. It should be noted that in the limit of small σ_c and/or small α_{2D}, the α_{2D} term can

be dropped from (1.5*a*). Doing so yields partial cavity and supercavity solutions in terms of a single dimensionless ratio $\Psi = \sigma_c/2\alpha_{2D}$. The solutions L_c/c and $\partial C_{l_{2D}}/\partial\alpha_{2D}$ are plotted against Ψ in figures 2(*a*) and 2(*b*) respectively. Both solutions become pathological at $L_c/c = 1$, which is a mathematical artefact that results from the use of the hodograph transformation. Brennen (1995) suggests that the correct behaviour of a cavitating hydrofoil can be inferred by removing a section of each solution near $L_c/c \approx 1$. In order to find a single smooth approximation of the cavity length and lift spanning both solutions, rational polynomials are fitted through the linear solutions for supercavitation where $L_c/c \geqslant 1.25$ and partial cavitation where $L_c/c < 0.5$. Fitting yields that the dimensionless cavity length is approximated by

$$\frac{L_c}{c} = \frac{2.67\Psi + 96.62}{\Psi^3 - 7.1\Psi^2 + 49.42\Psi + 0.961}. \tag{1.7}$$

A lower-order fit, which approximates L_c/c with a single term, is

$$\frac{L_c}{c} \approx \frac{2.31}{\Psi} = 4.62\frac{\alpha_{2D}}{\sigma_c}. \tag{1.8}$$

The slope of the lift coefficient curve is fitted by

$$a_0 = \frac{\dfrac{\pi}{2}\left(\dfrac{L_c}{c}\right)^3 - 2\left(\dfrac{L_c}{c}\right)^2 + 4.5\left(\dfrac{L_c}{c}\right) + 1}{\left(\dfrac{L_c}{c}\right)^3 - \left(\dfrac{L_c}{c}\right)^2 + 0.75\left(\dfrac{L_c}{c}\right) + \dfrac{1}{2\pi}}, \tag{1.9}$$

which approaches the respective analytical solutions in the limits ($a_0 = 2\pi$ as $L_c/c \to 0$ and $\pi/2$ as $L_c/c \to \infty$). Equations (1.7)–(1.9) are also plotted in figure 2(*a*,*b*).

1.2.2. *Lifting-line model of three-dimensional cavity flows*

To extend the concepts of 2D cavity flows to a 3D topology, a simple lifting-line model is used next to illustrate the effects of gravity and finite aspect ratio. Consider a hydrofoil that vertically pierces the free surface, as shown schematically in figure 3. A horizontal section cut may be taken through the hydrofoil at a depth of $z' = -(S - h) - Z$ below the free surface, where S is the total span of the hydrofoil and Z is defined pointing upward from the hydrofoil root (away from the water surface). In the plane of this cut, the cavitation number can be recast as (Young & Brizzolara 2013)

$$\sigma_c(z') = \frac{P_{atm} + \rho g z' - P_c}{1/2\rho u^2} = \Delta\sigma + \frac{z'}{h}\frac{2}{Fn_h^2}, \tag{1.10}$$

where

$$\Delta\sigma = \frac{P_{atm} - P_c}{\rho u/2}. \tag{1.11}$$

For the case of natural ventilation, the cavity is open to the atmosphere, so $P_c = P_{atm}$ and $\Delta\sigma = 0$, leading to the expression

$$\sigma_c(z') = \frac{z'}{h}\frac{2}{Fn_h^2}, \tag{1.12}$$

which increases linearly with depth for a given Fn_h, as shown in figure 3 by the dashed line.

The presence of the free surface and the finite aspect ratio lead to non-uniform distribution of sectional effective angles of attack along the spanwise (Z) axis,

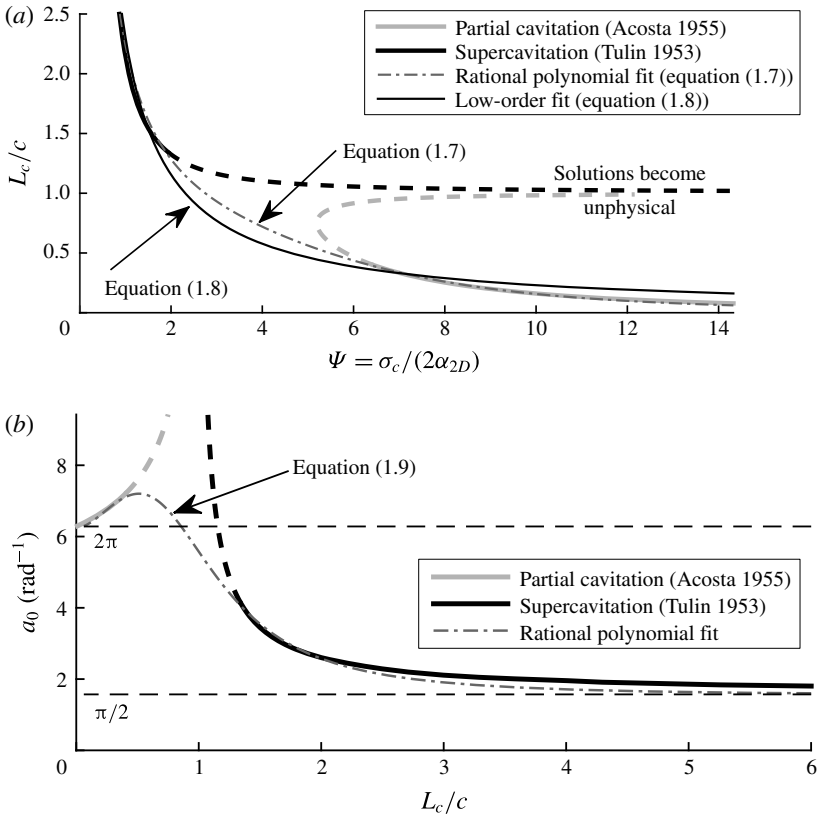

FIGURE 2. Modelling of sectional (*a*) cavity length and (*b*) lift-curve slope. (*a*) Dimensionless cavity length plotted against cavitation parameter Ψ. The exact form of (1.5*a*) is shown for $\alpha_{2D} = 4°$. The dashed segments indicate portions of the linear solutions that approach non-physical singularities at $L_c/c = 1$, and which are not used for fitting. A rational polynomial and a single-term expression are shown to smoothly approximate the valid regions of both classical expressions. (*b*) Sectional lift coefficient slope (a_0), plotted against dimensionless cavity length. A rational polynomial is fitted through the valid portions of the linear solutions to yield a smooth explicit equation that approaches the analytical values of 2π and $\pi/2$ in the limits of $L_c/c \to 0$ and $L_c/c \to \infty$ respectively.

i.e. $\alpha_{2D}(Z) \neq \alpha$. The discrete lifting-line code shown by Harwood & Young (2014) is modified to model surface-piercing lifting bodies in ventilated flows. An abbreviated description of the modified lifting-line model follows; more details on the original form of the method may be found in Harwood & Young (2014).

The lifting-line formulation collapses a 3D wing onto a 1D spanwise distribution of section properties. Glauert (1943) presented the following governing equations, which relate the induced downwash velocity $v(Z)$ and bound circulation $\Gamma(Z)$:

$$v(Z) = \int_0^S \frac{\partial \Gamma(\zeta)}{\partial \zeta} \frac{1}{4\pi(\zeta - Z)} \partial\zeta, \tag{1.13}$$

$$\Gamma(Z) = \frac{c(Z)}{2}[a_0(u(Z)\alpha(Z) + v(Z)) + C_{l_0}u(Z)], \tag{1.14}$$

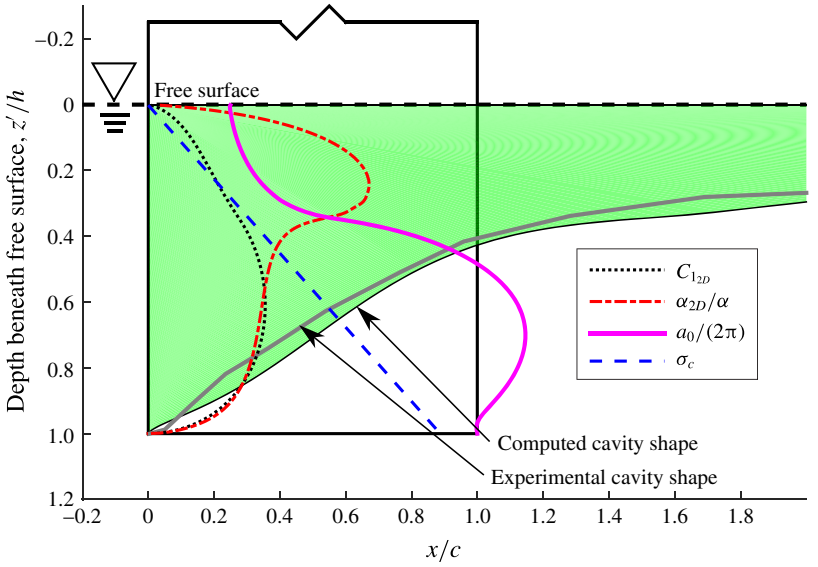

FIGURE 3. (Colour online) Nonlinear lifting-line model of a surface-piercing hydrofoil at $\alpha = 10°$, $Fn_h = 1.5$, $AR_h = 1.0$. The suction surface of the hydrofoil is shown. The effective angle of attack and cavitation number both vary along the span, leading to a spanwise non-uniform cavity. The agreement between computed and true cavity profiles (observed in the present experimental study) suggests that the simplistic model is suitable for capturing qualitative features of 3D ventilated cavity flows.

where α is the local section geometric angle of attack and C_{l_0} is the 2D lift coefficient at $\alpha = 0°$. The two equations may be combined into the fundamental integral equation for the circulation distribution, which must be satisfied at all points on the lifting line:

$$\int_0^S -\frac{\partial \Gamma(\zeta)}{\partial \zeta}\frac{1}{4\pi(\zeta - Z)}\partial\zeta + \frac{2\Gamma(Z)}{a_0 c} = u(Z)\left[\alpha(Z) + \frac{C_{l_0}}{a_0}\right]. \tag{1.15}$$

In this work, the governing equation is recast as a root-finding problem and the small-angle assumption is removed, giving

$$\frac{v(Z)}{u(Z)} + \sin(\alpha(Z)) - \sin(\alpha_{2D}(Z)) = 0. \tag{1.16}$$

Equation (1.16) states that the effective angle of attack of a section (α_{2D}) is a sum of the geometric angle of attack (α) and the dimensionless downwash induced at that section (v/u). Downwash is the name given to flow normal to the surface of the hydrofoil (along the positive Y axis as defined in figure 1), induced by vorticity shed from neighbouring sections. The span of the hydrofoil is discretized into panels, at the centre of each of which (1.16) is imposed. The derivative term present in (1.15) is approximated with finite differences (second-order central and backwards differencing), and the integral term is approximated by trapezoidal quadrature. The lift coefficient and bound circulation of a 2D section are related by

$$\Gamma(Z) = C_{l_{2D}}(Z)\frac{u(Z)c(Z)}{2}. \tag{1.17}$$

Equation (1.13), rewritten in the compact discrete form, gives

$$\boldsymbol{v} = -\boldsymbol{\Omega}\boldsymbol{\Gamma} = -\tfrac{1}{2}\boldsymbol{U}^D\boldsymbol{c}^D\boldsymbol{\Omega}\boldsymbol{C}_{l_{2D}}. \tag{1.18}$$

For a hydrofoil discretized at N stations, $\boldsymbol{\Omega}$ is an $N \times N$ matrix operator containing the differencing and quadrature weights, $\boldsymbol{c}^D$ and $\boldsymbol{U}^D$ are diagonal $N \times N$ matrices with entries respectively corresponding to the chord and inflow velocities of each of the N sections, and $\boldsymbol{C}_{l_{2D}}$ and $\boldsymbol{v}$ are each an $N \times 1$ column vector containing the sectional lift coefficients and induced downwash velocities of the sections respectively.

By substituting (1.18) into (1.16), the following system is derived:

$$\tfrac{1}{2}\boldsymbol{\Omega}\boldsymbol{c}^D\boldsymbol{C}_{l_{2D}} + \sin(\boldsymbol{\alpha}_{2D}) - \sin(\boldsymbol{\alpha}) = \boldsymbol{0}. \tag{1.19}$$

Equation (1.19) is solved by iterating on $\boldsymbol{\alpha}_{2D}$ using a numerical root-finding algorithm.

In (1.18) and (1.19), the vector $\boldsymbol{C}_{l_{2D}}$ must be computed as some function of the known section parameters. Following the 2D cavitating-flow models in § 1.2.1, $\boldsymbol{C}_{l_{2D}}$ is made a function of the respective sectional α_{2D} and σ_c. For a given distribution of α_{2D} and with σ_c known at each spanwise section (via (1.12)), the distribution of L_c/c is estimated by applying (1.7) to the calculated distributions of α_{2D} and σ_c. Equation (1.9) is then used to calculate the unscaled 2D lift coefficient distribution, $C^*_{l_{2D}}$. The lifting line does not fully capture 3D effects for very small aspect ratios because it neglects effect such as cross-flow. Small immersed aspect ratios are being considered in the present work, so a correction factor is used to rescale the sectional distribution as a means of approximating the additional 3D effects. Helmbold (1942) derived the expression for the total lift of rectangular wings of small aspect ratio ($AR < 4$) as

$$C_L^H = \left[\frac{a_0}{\dfrac{a_0}{\pi AR} + \sqrt{1 + \left(\dfrac{a_0}{\pi AR}\right)^2}}\right]\alpha. \tag{1.20}$$

Equation (1.20) is used to rescale the computed $\boldsymbol{C}^*_{l_{2D}}$ for small aspect ratios, inside of the iterative solution of (1.19). At each iteration, the unscaled 3D lift coefficient (C^*_L) is computed by integrating $C_{l_{2D}}$ along the span,

$$C^*_L = \frac{1}{h}\int_0^h C_{l_{2D}}(z')\,\mathrm{d}z'. \tag{1.21}$$

The lift slope, a_0, also varies along the span. To find a single representative value for use in (1.20), a lift-weighted mean value (a_0^*) is estimated from the lifting-line results,

$$a_0^* = \frac{1}{hC^*_L}\int_0^h \frac{C^*_{l_{2D}}(z')^2}{\alpha^*_{2D}(z')}\,\mathrm{d}z'. \tag{1.22}$$

Numerical quadrature is used to evaluate (1.21) and (1.22). The lift-weighted mean value a_0^* is substituted into (1.20) to yield the scaled 3D lift coefficient C_L^H. The Helmbold correction factor H is computed as the ratio

$$H = \frac{C_L^H}{C^*_L}. \tag{1.23}$$

Finally, the 2D lift distribution is rescaled,

$$\boldsymbol{C}_{l_{2D}} = H\boldsymbol{C}^{*}_{l_{2D}}. \tag{1.24}$$

The vector $\boldsymbol{C}_{l_{2D}}$ is then substituted into (1.19). By executing this procedure at each iteration, equation (1.19) may be iteratively solved for $\boldsymbol{\alpha}_{2D}$.

A zero-load boundary condition is imposed at the foil tip and a negative image of the vorticity distribution is imposed above the free surface, forcing the effective angle of attack, $\alpha_{2D}(z')$, to be zero at $z' = 0$ and $z' = h$. The negative image method can be formulated by imposing the linearized dynamic/kinematic free-surface boundary condition for large chord-based Froude numbers. Boundary conditions are built into the matrix operator $\boldsymbol{\Omega}$. More details on image techniques are given by Faltinsen (2005), and the inclusion of images in the coefficient matrix is described by Harwood & Young (2014).

The non-dimensional distributions of α_{2D}/α, L_c/c, $a_0/(2\pi)$, σ_c and $C_{l_{2D}}$ are shown in figure 3 for a case of $\alpha = 10°$, $Fn_h = 1.5$ and $AR_h = 1.0$. The planform of the ventilated cavity observed in experiments (described in § 2) at the same flow conditions is shown for comparison. The lifting-line method is not proposed as a high-fidelity model, but the close agreement between the computed and observed cavity profiles suggests that the inclusion of gravitational, free-surface and 3D effects adequately captures the dominant features of a 3D ventilated cavity flow around a surface-piercing hydrofoil. One should note the characteristic hump in the sectional angle of attack where the sections are supercavitating, which occurs because a_0 reduces sharply when $L_c/c > 1$, while $C_{l_{2D}}$ remains smooth and without major inflections. The shape of the a_0 distribution reflects that in figure 2(*b*), with a local maximum where sections are partially cavitating.

The cavity is clearly non-uniform along the span as a result of gravitational effects and the finite aspect ratio. Unlike the well-established topologies of 2D cavity flows, 3D cavity flows cannot be easily defined. Sections taken, for example, at $z' = 0.1h$, $z' = 0.5h$ and $z' = h$ in figure 3 would be respectively classified as supercavitating, partially cavitating and fully wetted under the classifications of figure 1. At transitional Froude numbers ($0.5 \leqslant Fn_h \leqslant 2$), the spanwise pressure gradient is of the same order as the chordwise pressure gradient, resulting in the strongly 3D topology. Such flows have been described in the literature either using *ad hoc* terminology or by considering only a representative 2D section of a 3D geometry. As a result, the distinction between partial ventilation and full ventilation becomes ambiguous for 3D geometries at low-to-moderate Froude numbers, requiring a more quantitative set of criteria for delineating flow regimes in a laboratory environment.

1.2.3. *Summary*

The example presented in § 1.2 demonstrates that combined 3D effects, free-surface effects and gravity can yield cavity profiles at moderate Froude numbers that are not suitably described by the 2D terminology found in the literature. An adequate characterization of 3D cavity flows is still needed, particularly at low-to-moderate Froude numbers. Moreover, there is a need to identify the mechanisms that cause transition between steady flow regimes and when these ventilation transition processes occur. Previous studies have focused on the steady regimes of ventilated flows and the resulting steady lift and drag forces. Those studies that have dealt with unsteady ventilation transition mechanisms have focused almost exclusively on formation mechanisms, leaving the processes of ventilation elimination unexplored.

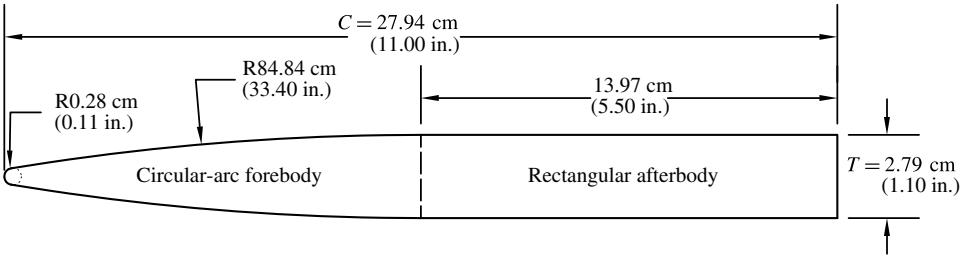

FIGURE 4. Cross-section of the hydrofoil. The model was machined from 6061 aluminium.

2. Experimental set-up

To address the issues described above, a study was performed on a canonical surface-piercing hydrofoil. The work is focused on a region of low-to-moderate Froude numbers and Reynolds numbers, where both gravitational and viscous forces are significant, and in which large changes in hydrodynamic loading and flow topology occur. Experiments were carried out in the towing tank at the University of Michigan Marine Hydrodynamics Laboratory, which has dimensions of 110 m (360 ft) long $\times$ 6.7 m (22 ft) wide $\times$ 3.05 m (10 ft) deep. The model was towed by a gantry-type carriage, capable of speeds of up to 6.1 m s^{-1} (20 ft s^{-1}).

2.1. *Experimental model and fixture*

The model used in the experiments possesses a uniform semi-ogival section along the span, with a 27.94 cm chord and a maximum thickness of 2.79 cm, a circular-arc (ogival) forebody with a radius of curvature of 84.84 cm, and a rectangular afterbody. The section has a leading edge radius of $0.01c$ and a blunt trailing edge, as shown in figure 4. The hydrofoil has a rectangular planform with a 91 cm span, and was machined as a single piece from 6061 aluminium. The geometry resembles that used in past studies, particularly the models of Waid (1968), Rothblum *et al.* (1969) and Swales *et al.* (1973, 1974).

The hydrofoil was clamped at the root and slung vertically in a cantilevered configuration to pierce the water free surface, as shown in figure 5. A steel fixture frame was mounted between two longitudinal structural members of the towing-tank carriage (figure 5*b*). Threaded feet were used to bring the frame to within $\pm 0.1^\circ$ of level, as measured in the X–Z and Y–Z planes. The hydrofoil was coupled to the frame by way of a load cell that, in turn, attached to a drum that rotated about a vertical axis, permitting the yaw angle (angle of attack) to be varied. An ATI Omega-190 US 800-6000 six-degree-of-freedom force–torque transducer was used to measure forces and moments at the root of the hydrofoil.

2.2. *Videography and surface-flow visualization*

Videography was performed using GoPro® brand cameras (HERO3 Black® models) in waterproof housings. Video was recorded with a resolution of 1920 $\times$ 1080 pixels at a rate of 60 frames s^{-1}. Lighting was provided by commercial halogen work lamps mounted below the carriage and aimed at the hydrofoil. Video streams were recorded above and below the water and were collectively synchronized with the data collection by an LED indicator in the field of view of each camera.

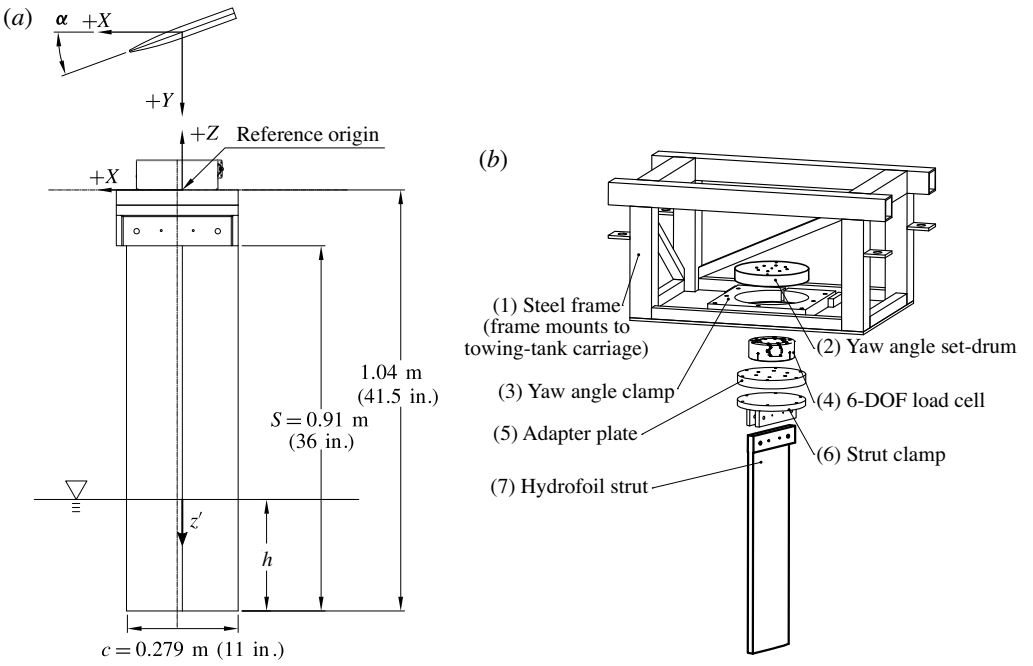

FIGURE 5. Experimental apparatus for the surface-piercing foil experiments. (*a*) The foil geometry, foil dimensions and coordinate system used in the following discussion. (*b*) An exploded view of the components comprising the experimental rig. The entire apparatus attaches to the towing-tank carriage.

A limited number of surface-flow visualizations were conducted using a grid of paint dots, following the method of Green (1988) and Green & Acosta (1991). Eight parts yellow artist's oil paint and one part white oil primer were mixed with five to twelve parts refined linseed oil to achieve a range of shear-thinning behaviours, suitable for trials conducted at different speeds. Droplets of volume 10 μL were applied as a grid on the suction surface of the hydrofoil with a pipette, with a spacing of approximately 1–2.5 cm (0.5–1 in.), totalling between 50 and 150 dots. Between each trial, the foil was wiped clean and the dots were reapplied.

2.3. *Experimental procedure*

The yaw angle, or angle of attack (α), was measured as the rotation of the hydrofoil in the X–Y plane. The yaw angle α was set by visually sighting one-degree marks machined into the yaw drum (see figure 5) against a reference line calibrated to match the longitudinal axis of the towing tank. The drum was secured by tightening a collar clamp. The depth of immersion was varied by adding and draining water from the towing tank and visually sighting the water line against tick marks drawn along the span of the hydrofoil. Speed was measured by an optical encoder wheel, and instantaneous carriage speed was governed by an on-board controller. The variable U_∞ denotes the steady-state speed entered as an input to the carriage speed controller, while $u(t)$ is the instantaneous velocity of the carriage, measured by the optical encoder. During a run, the carriage accelerated to the specified speed ($u(t) = U_\infty$) and decelerated again along a programmed speed profile. The acceleration

Chord length	c	0.279 m	(11 in.)
Foil span	S	0.914 m	(36 in.)
Maximum thickness	T	0.0279 m	(1.1 in.)
Tip immersion	h	0.14, 0.28, 0.41 m	(5.5, 11, 16.5 in.)
Immersed aspect ratio	$AR_h = \frac{h}{c}$	0.5, 1.0, 1.5	
Steady velocities	U_∞	0.6–6 m s^{-1}	(1.8–20 ft s^{-1})
Depth Froude number	$Fn_h = \frac{u}{\sqrt{gh}}$	0.5–5	
Chord Reynolds number	$Re_c = \frac{uc}{\nu}$	1.5×10^5–1.7×10^6	
Yaw angle	α	$-5^\circ - 30^\circ$	
Weber number	$We = \frac{\rho u^2 c}{\gamma}$	1.2×10^3–1.42×10^5	
Vaporous cavitation number	$\sigma_v = \frac{P_{atm} - P_v}{1/2\rho u^2}$	5.4–540	

TABLE 2. Model dimensions and ranges of variables used in the present experiment.

of the carriage during the ramp-up and ramp-down stages was software-limited to ± 0.025–0.525 m s^{-2}. The ranges of parameters investigated are given in table 2. Trials were conducted by varying U_∞ for each configuration of α and AR_h, then varying α within each fixed value of AR_h, and varying AR_h once all values of α and Fn_h had been tested.

For each trial, data collection was started while the carriage was at rest. For steady-state data collection, ramp-up and ramp-down times were minimized to increase the amount of data collected at the target condition of $u(t) = U_\infty$. To study formation, elimination and other transient processes, the ramp-up and/or ramp-down times were typically made longer to minimize inertial effects. A small-diameter air jet (driven by a pneumatic tank at 350–700 kPa) was used to perturb the flow at the junction of the free surface and the foil leading edge in order to trigger ventilation at small yaw angles. Airflow through the jet was actuated by a solenoid valve, in turn controlled by an output from the data acquisition computer. The valve was set to open when $u(t)$ remained within $\pm 3\,\%$ of U_∞ continuously for a user-specified period of time, and to remain open for a user-specified duration. The duration of air injection was varied between 0.25 and 1 s as needed to achieve ventilation. Sufficient time (5–15 min) was permitted between runs to allow waves and currents in the tank to dissipate.

2.4. *Data collection and processing*

The speed and load-cell outputs were recorded using a pair of 16-bit National Instruments multifunction DAQ cards on either a PCI-e bus or a dedicated PXI chassis. All signals were sampled at 1000 Hz, with asynchronism of less than 1 μs introduced by channel muxing on the analogue-to-digital converters (ADCs). All voltage signals were normalized to a ± 10 volt range to maximize the dynamic range of the ADCs.

Windows around steady-state data were manually specified. In some cases, a short window was taken on data recorded during acceleration or deceleration phases. Data

	Maximum measurement uncertainties	
α	Yaw angle	$\pm 0.25^{\circ}$
U_∞	Steady forward speed	$\pm 0.5\,\%$
$u(t)$	Instantaneous forward speed	$\pm 3\,\%$
$F_{X,Y,Z}$	X, Y, Z forces	$\pm 3.3\,\%$
$M_{X,Y,Z}$	X, Y, Z moments	$\pm 2.3\,\%$
h	Tip immersion depth	± 0.6 cm (± 0.25 in.)
t_v	Video synchronization time	± 0.016 s ($\pm$ one frame)
	Maximum propagated uncertainties	
AR_h	Immersed aspect ratio	± 0.023
Fn_h	Depth Froude number	$AR_h = 0.5 \rightarrow \pm 5.4\,\%$ $AR_h = 1.0 \rightarrow \pm 4.2\,\%$ $AR_h = 1.5 \rightarrow \pm 3.8\,\%$
C_L, C_D	Lift, drag coefficients	$AR_h = 0.5 \rightarrow \pm 15\,\%$ $AR_h = 1.0 \rightarrow \pm 12.5\,\%$ $AR_h = 1.5 \rightarrow \pm 11.6\,\%$
C_M	Moment coefficient	$AR_h = 0.5 \rightarrow \pm 14\,\%$ $AR_h = 1.0 \rightarrow \pm 11.4\,\%$ $AR_h = 1.5 \rightarrow \pm 10.5\,\%$

TABLE 3. Nominal error bounds of measured quantities are given in the first section. Values are quoted from the load-cell manufacturer in the case of forces and moments, estimated from recorded data in the case of speed, and taken to be one quarter of the smallest delineation for yaw angle and tip immersion. It should be noted that force/torque uncertainties are quoted at 50 % of the rated load, and include cumulative noise and quantization error. Propagated uncertainty bounds on quantities of interest are given in the second part. It should be noted that different values are given, corresponding to the three immersed aspect ratios that were tested.

taken during transient flows were considered to be suitably quasi-steady when no significant topological changes were observed and when all recorded speeds remained within $\pm 3\,\%$ of the desired steady velocity during the window in question. In other words, a time window t_w was specified as $t_w = \{t \mid u(t)$ within $\pm 3\,\%$ of $U_\infty\}$. In this way, slowly varying ramped runs were used to canvas several quasi-steady flow conditions in a single run. Statistics for speed, force and moment coefficients, instantaneous accelerations, and other inferred quantities were calculated on these windows. Some transient effects, due to fluid inertia, are unavoidable. However, for $Fn_h > 1$, the effect of unsteady inertial fluid loading on measured lift and drag may be neglected. The justification for this statement can be found in appendix B. The nominal uncertainty bounds of measured quantities and the propagated uncertainty in results of interest are presented in table 3.

3. Results: steady flows

In this section, the flow structure of steady ventilation is described. The role of the re-entrant jet is described in § 3.1. Characteristic flow regimes are classified in § 3.2, and their effects on the hydrofoil hydrodynamic loading are given in § 3.3. The stability boundaries of the regimes are mapped in § 3.4.

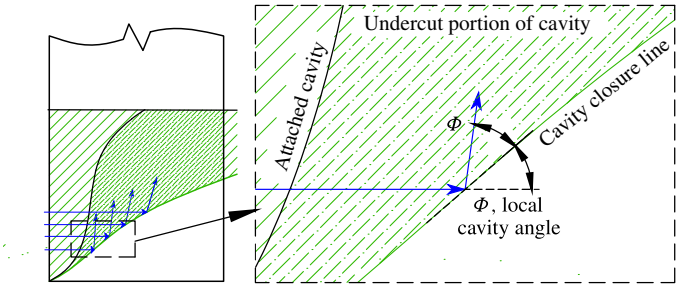

FIGURE 6. (Colour online) Schematic representation of the re-entrant jet on a spanwise-varying cavity. When incoming flow (arrows) encounters an oblique line of cavity closure at a local angle Φ, the flow is reflected about the normal to the cavity closure line so that the resulting jet spray is directed along an angle of 2Φ from the horizontal plane.

3.1. *The re-entrant jet at cavity closure*

Where a cavity closes on a solid surface, streamlines inside the stagnation streamline form a jet spray that undercuts the cavity, known as a re-entrant jet (Laberteaux & Ceccio 2001*a*). In 2D flows, the re-entrant jet may impinge on the upstream cavity boundary, causing 'pinch-off'. A well-known example is the phenomenon of sheet–cloud cavitation, which occurs when a re-entrant jet induces periodic shedding of vaporous partial cavities. When the line of cavity closure is non-normal to the incoming flow, the re-entrant jet is a reflection of the incoming flow about the cavity closure line, as shown in figure 6 (De Lange & De Bruin 1998; Laberteaux & Ceccio 2001*b*; Franc & Michel 2006). If incoming flow encounters a cavity closure line at a local angle of Φ from the horizontal plane, the jet flow will be directed at an angle of 2Φ, as shown by the arrows in figure 6. At a given depth beneath the free surface, z', the magnitude of the jet velocity vector ($\boldsymbol{U}_j$) may be obtained by applying Bernoulli's equation between the upstream flow (known velocity) and the cavity boundary (known pressure) to obtain

$$\|\boldsymbol{U}_j(z')\| = u\sqrt{1+\sigma_c(z')}. \tag{3.1}$$

The respective streamwise (U_j) and spanwise (W_j) components of the re-entrant jet velocity are (Harwood *et al.* 2014)

$$U_j(z') = U_0\sqrt{1+\sigma_c(z')}\cos(2\Phi(z')), \tag{3.2a}$$

$$W_j(z') = U_0\sqrt{1+\sigma_c(z')}\sin(2\Phi(z')). \tag{3.2b}$$

It should be noted that these velocities are derived from the steady Bernoulli equation, which neglects viscosity, and so may be valid only at the cavity closure line where the jet develops. Callenaere *et al.* (2001) pointed out that viscosity probably slows the re-entrant jet down somewhat, especially for very thin cavities. Thick cavities, however, lead to thick re-entrant jets, which possess enough momentum that reductions in jet speed by skin friction may be neglected. For the purposes of this discussion, it is assumed that the jet is sufficiently thick for $\alpha \geqslant 5°$ to preclude its stagnation by skin friction. As a result, the direction of the jet, rather than the velocity, is of primary interest.

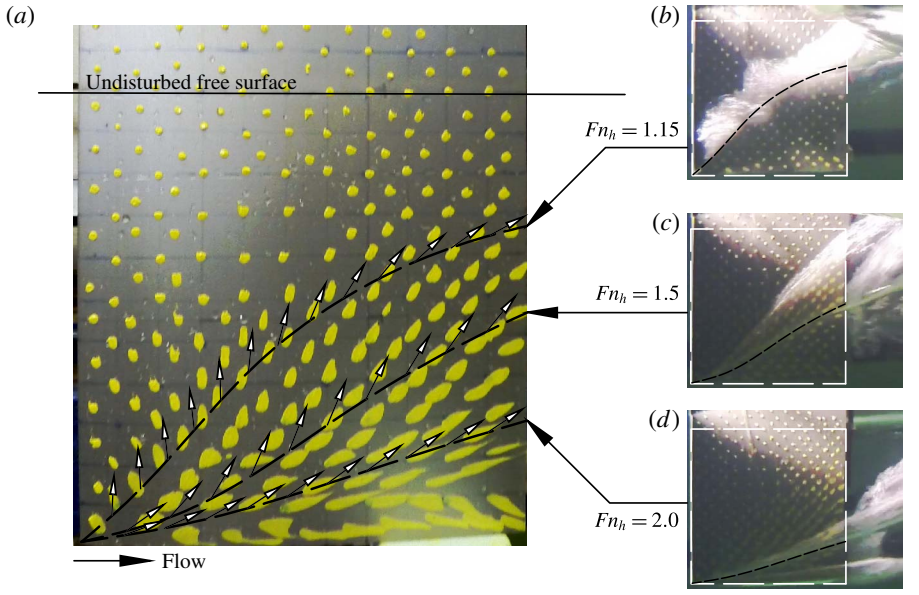

FIGURE 7. (Colour online) Paint streaks on the suction side of a hydrofoil in accelerating flow at $\alpha = 14°$, $AR_h = 1$. As the speed increased, the cavity grew (see *b–d*), sweeping the re-entrant jet over the surface of the foil and shearing the paint in the direction of the jet. Cavity profiles are drawn for $Fn_h = 1.15$, 1.5 and 2.0. Superimposed on each cavity profile are arrows indicating the local theoretical re-entrant jet direction of 2Φ. The streaks in the paint coincide with the theoretical jet directions, indicating that the theory ((3.2*a*) and (3.2*b*)) correctly predicts the trajectory of the re-entrant flow.

The notion of re-entrant as a reflection of incoming flow is reinforced by the surface-flow visualization shown in figure 7. Paint dots were applied as described in § 2.2, and the hydrofoil was accelerated along a ramped velocity profile at a yaw angle sufficiently large for a ventilated cavity to spontaneously develop ($\alpha = 14°$). As the forward velocity, u, increased, the ventilated cavity grew in size. The re-entrant jet at the cavity closure line was swept over the paint dots, causing the dots to shear in the direction of the local jet spray. Some smearing of the dots was unavoidable, as the dots were sheared somewhat in the streamwise direction prior to their interaction with the re-entrant jet; nevertheless, the primary directions of streaking clearly coincide with the superimposed arrows, which indicate the local 2Φ trajectories at their intersections with the respective cavity profiles.

When the local angle of the cavity closure line is $\Phi > 45°$, the re-entrant jet will possess an upstream velocity component. With enough momentum, the jet impinges on the leading edge of the ventilated cavity, causing a large-scale shedding of the cavity via pinch-off (as in the case of sheet–cloud cavitation, described earlier). If this occurs over a significant portion of the span, then a ventilated cavity becomes unstable.

At this point, it is useful to define stability in the context of ventilated flows. If a configuration, or regime, of the flow remains unchanged following any perturbation to the flow, then that regime is considered to be exclusively and globally stable. If small perturbations do not affect the flow regime, but large perturbations cause transition to another flow regime, then the regime is considered to be locally stable. The coexistence of a locally stable regime and another locally or globally stable

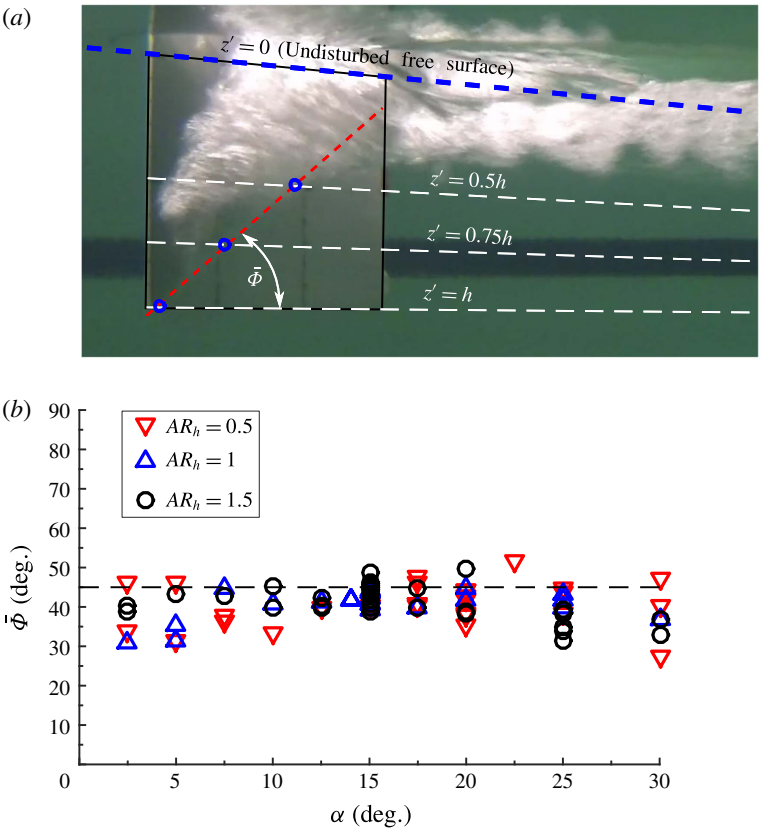

FIGURE 8. (Colour online) Experimental quantification of cavity closure angles at the point of cavity instability via pinch-off for immersed aspect ratios of $AR_h = 0.5$, 1 and 1.5. The example shown in (*a*) is at $Fn_h = 1.5$, $\alpha = 20°$, $AR_h = 1.0$. Cavity closure line profiles were linearly approximated to find $\bar{\Phi}$ at the instant of cavity instability. (*b*) Angles of cavity closure lines as a function of and AR_h. The mean value of $\bar{\Phi}$ is 40.75° and the dashed line corresponds to the proposed stability criterion of 45°.

regime constitutes a bi-stable set of conditions. For given flow conditions, a flow regime is considered to be unstable if it cannot be sustained, even if left unperturbed.

A criterion of $\bar{\Phi} = 45°$ is proposed on the stability of fully ventilated cavities, where $\bar{\Phi}$ is the angle of a linear approximation to the cavity closure line. To verify that $\bar{\Phi}$ is a suitable metric, images were taken of ventilated cavities in decelerating flows, immediately preceding the instant when the cavity became unstable. The cavity length was measured at three spanwise stations, as shown in figure 8(*a*), through which was fitted an affine curve to get the value of $\bar{\Phi}$, measured from the horizontal plane. The criterion $\bar{\Phi}$ is plotted as a function of α and AR_h in figure 8(*b*). Measurements were translated into real-world coordinates by using an inverse projective transform. The results show the cavity angle at washout to be tightly clustered around a mean of $\bar{\Phi} \approx 41°$ for all values of α and AR_h, which is acceptably close to the proposed stability boundary at $\bar{\Phi} = 45°$. With this stability condition, the topology of a cavity may be used to unambiguously distinguish partial ventilation from full ventilation in 3D flows.

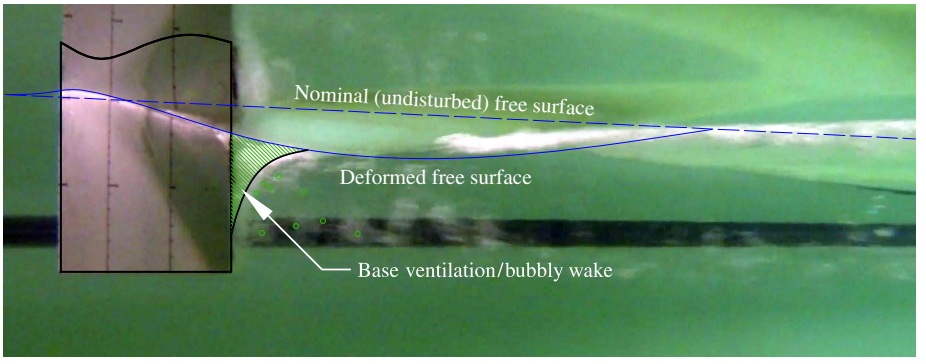

FIGURE 9. (Colour online) Fully wetted flow at $\alpha = 10°$, $Fn_h = 2$, $AR_h = 1.0$. The FW regime shows no entrainment of air along the suction surface ($D = 0$, as measured from the nominal free surface). Some base ventilation occurs aft of the blunt trailing edge of the foil.

3.2. *Flow-regime criteria*

Fully wetted (FW) flow is defined as the regime in which no pronounced entrainment of gas occurs. In the present experiments, a small aerated base cavity was typically observed in the separated wake of the blunt trailing edge. However, the effects of the trailing edge were confined to a relatively small region immediately aft of the trailing edge; neither the flow separation nor the base cavity materially affected the hydrodynamic response of the hydrofoil (Perry 1955). An example of FW flow is shown in figure 9. The nominal free surface indicates the initial calm water surface identified by the $z' = 0$ plane, where it intersects with the suction surface of the foil. The free-surface profile changes when subjected to the pressure distribution around the hydrofoil, and is termed the 'deformed' free surface.

Fully ventilated (FV) flow is defined as the case where a cavity is entrained along the entire immersed span of the hydrofoil suction surface ($D = h$, where D is the maximum depth of the ventilated cavity beneath the nominal free surface), and where no inherently destabilizing re-entrant jet occurs ($\bar{\Phi} < 45°$). Figure 10 shows an example of a fully ventilated cavity. The suction surface of the hydrofoil (pictured) is enveloped entirely inside a ventilated cavity. The near wall of the cavity detaches from the leading edge of the hydrofoil. The pressure side of the hydrofoil is fully wetted, and flow detaches smoothly from the corner of the pressure side and trailing edge to form the opposing cavity wall. Large spray sheets develop on both sides of the hydrofoil; the lower edge of the suction-side spray sheet is visible in figure 10. It should be noted that the angle of the cavity closure line is very shallow ($\bar{\Phi} \ll 45°$). As a result, the streamwise component of any re-entrant flow is directed towards the trailing edge of the hydrofoil, where it presents no detriment to the cavity stability. In figure 10, a strong tip vortex is present, the core of which aerates by ingesting air from the cavity. When the flow is in a fully ventilated state, the blunt trailing edge is contained entirely within the cavity, so it does not interact with the liquid flow. In the case pictured, and in other cases with a sufficiently strong tip vortex, the circumferential flow around the vortex impinges on the near (as pictured) cavity wall, forcing a small jet horizontally across the cavity. The impact of this jet on the far cavity wall causes a vertical jet spray to develop in the ventilated wake.

Partially ventilated (PV) flow is defined as the entrainment of a cavity which either does not span the entire immersed portion of the hydrofoil or does not meet the

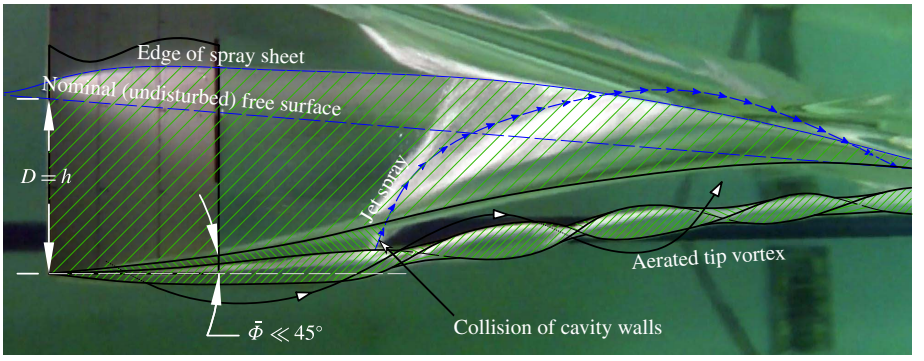

FIGURE 10. (Colour online) Fully ventilated flow at $\alpha = 15°$, $Fn_h = 3.0$, $AR_h = 1.0$. The suction surface (pictured) is contained entirely within the walls of the cavity. The cavity satisfies both FV flow criteria ($D = h$ and $\bar{\Phi} \leqslant 45°$). In the case pictured, a strong tip vortex is present, the core of which aerates by ingesting air from the cavity.

stability conditions to sustain fully ventilated flow (e.g. a destabilizing re-entrant jet exists). Figure 11 depicts two examples of partial ventilation. The flow in figure 11(*a*) is designated PV because the cavity does not reach the immersed tip of the hydrofoil ($D < h$). In this case, the cavity depth and length are potentially unsteady. The flow pictured in figure 11(*b*) is so designated because the approximate cavity closure line, shown as a solid line fitted through the cavity closure region, exceeds the $\bar{\Phi} = 45°$ stability condition, which is indicated by the dashed white line. As a result, a significant portion of the re-entrant jet is directed towards the leading edge. At small angles of attack, the resulting upstream flow may cause unsteady shedding of bubbly structures in a region confined to the trailing edge of the cavity, while at larger angles of attack, the jet destabilizes the entire cavity by impinging on the cavity interface and leading to pinch-off. In either case, the increased unsteadiness and decreased stability of the flow when $\bar{\Phi} \geqslant 45°$ serve to distinguish it from FV flow.

The criteria for the three flow regimes may be summarized as follows:

$$D = 0, \quad \text{fully wetted (FW) flow;}$$

$$D = h \quad \text{and} \quad \bar{\Phi} < 45°, \quad \text{fully ventilated (FV) flow;}$$

$$0 < D < h \quad \text{or} \quad \bar{\Phi} \geqslant 45°, \quad \text{partially ventilated (PV) flow.}$$

Here, D is the depth of a ventilated cavity, measured from the free surface, and $\bar{\Phi}$ is the approximate angle of the cavity closure line.

3.3. *Ventilation and hydrodynamic loading*

When ventilation occurs, most or all of a lifting-surface suction surface becomes encapsulated in a cavity. The pressure inside the cavity after ventilation occurs is, by necessity, higher than the local absolute pressure in the prior wetted flow. Suction pressures along the portions of the hydrofoil within the cavity are thus strongly attenuated. As a result, ventilation can induce dramatic reductions in realizable lift,

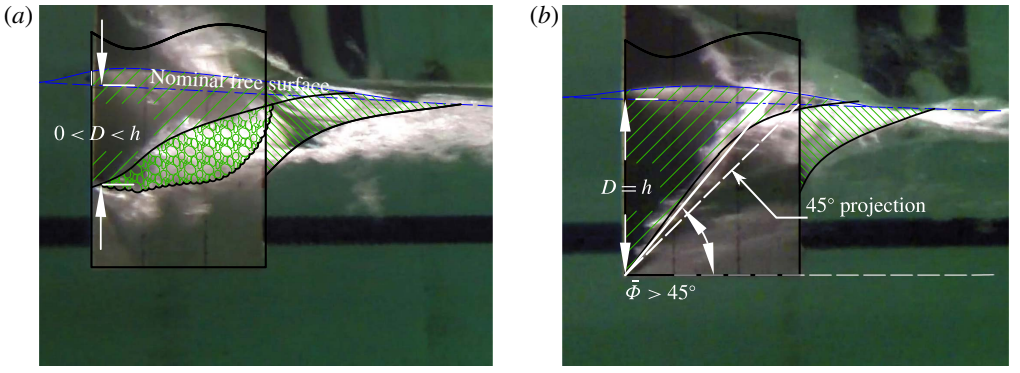

FIGURE 11. (Colour online) Partially ventilated flow, with (*a*) $\alpha = 20°$, $Fn_h = 1.0$, $AR_h = 1.0$; (*b*) $\alpha = 7.5°$, $Fn_h = 1.54$, $AR_h = 1.0$. (*a*) The case where the cavity does not reach the free tip ($0 < D < h$). (*b*) The case where the cavity reaches the free tip ($D = h$), but the angle of the solid line fitted through the cavity closure region is greater than the critical angle ($\bar{\Phi} = 45°$, shown as a dashed white line).

as observed by Breslin & Skalak (1959), Rothblum *et al.* (1969) and Swales *et al.* (1974). The 3D lift, drag and yawing moment coefficients are defined as

$$C_L = \frac{F_Y}{1/2\rho u^2 hc}, \tag{3.3a}$$

$$C_D = \frac{-F_X}{1/2\rho u^2 hc}, \tag{3.3b}$$

$$C_M = \frac{M_Z}{1/2\rho u^2 hc^2}. \tag{3.3c}$$

Here, F_X, F_Y and M_Z are taken with respect to the coordinate system shown in figures 1 and 5(*a*).

Figure 12 shows C_L in the FW and FV flow regimes; a distinctive grouping of the data into the two regimes is evident. The PV data are omitted for clarity, but may be found in appendix A. The lift in the FV regime is significantly lower than that in the FW regime, and the difference in lift between the two regimes tends to increase with increasing α. It should be noted that a line fitted to the FV data will have an apparent non-zero intercept because the profile of the foil pressure surface and the streamline bounding the cavity together present to the flow a cambered lifting surface (Breslin & Skalak 1959).

The nonlinear lifting-line model from § 1.2 was also used to approximate the lift. In the FV regime, the root-finding approach of § 1.2.2 was used to resolve the distributions of L_c/c, a_0, α_{2D} and $C_{l_{2D}}$ iteratively. In the FW regime, equation (1.7) was replaced with $L_c/c = 0$ and (1.9) was replaced with $a_0 = 2\pi$. In both regimes, the lifting-line model correctly captures the trends of the experimental measurements.

The drag coefficients are shown in figure 13. The dashed lines indicate the summed frictional and lift-induced drag coefficients from the lifting-line model. The skin friction coefficient was estimated via the ITTC 1957 correlation line (Larsson & Raven 2010) to be $C_{D_f} = 0.0047$ at the conditions in figure 13. The skin friction was integrated over both surfaces of the foil in the FW regime and over the pressure surface only in the FV regime. Breslin & Skalak (1959) posited that, for certain

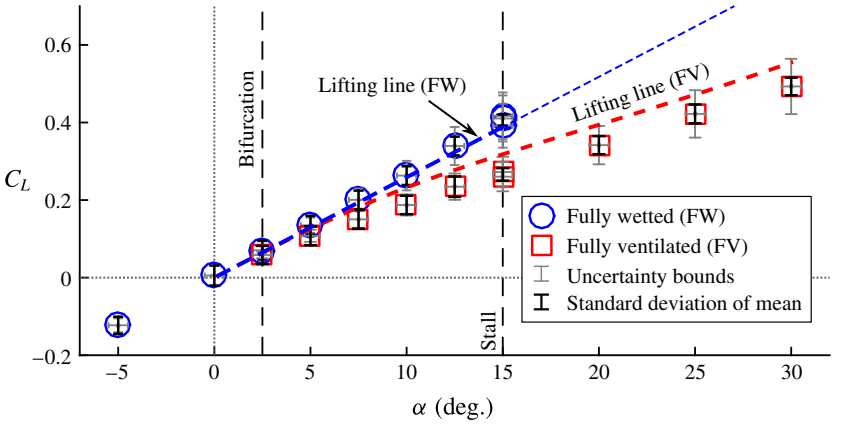

FIGURE 12. (Colour online) The 3D lift coefficient as a function of α at $Fn_h = 2.5$ and $AR_h = 1.0$. Propagated uncertainties from table 3 are shown as grey bars. Black bars are used to denote the standard deviation of C_L within the respective steady-state time window. Where duplicate points exist, the black bars correspond to the standard deviation of the estimate of the mean C_L. Between the bifurcation angle (α_b) and the stall angle (α_s), both wetted and ventilated flow regimes were observed, signalling a bi-stable range of α. The nonlinear lifting-line model calculations are also shown, with thin lines used to indicate predictions outside the experimentally observed ranges of α.

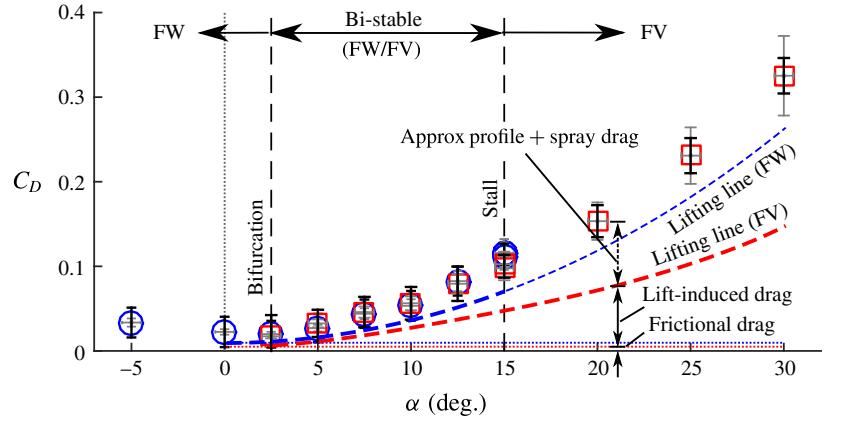

FIGURE 13. (Colour online) The 3D drag coefficients as a function of α at $Fn_h = 2.5$ and $AR_h = 1.0$. Both regimes exhibit a classical quadratic variation of C_D with α. The drag coefficients are nearly continuous between the two regimes. The results of the lifting-line model include induced and frictional drag only, suggesting that the increased profile drag and spray drag of the cavity roughly negate the reduction in frictional and induced drag.

geometries, a ventilated cavity yields an increased profile drag that roughly offsets the reduction in skin friction and induced drag. The frictional drag represents only a very minor contribution to the total drag in both regimes, so the near continuity of the measured total drag between the FW and FV flow regimes implies that any changes in the remaining components of drag (induced drag, profile drag, spray drag, etc.) approximately negate one another. The significant reduction in the induced

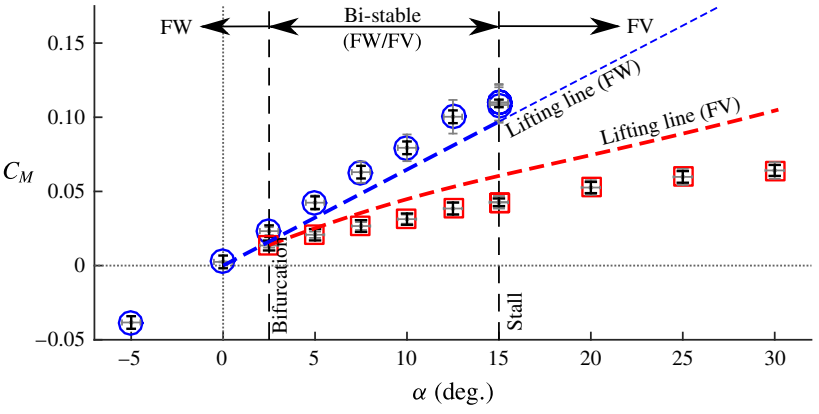

FIGURE 14. (Colour online) The 3D yawing moment coefficient as a function of α at $Fn_h = 2.5$ and $AR_h = 1.0$. The yawing moment is defined about mid-chord. It is strongly reduced in ventilated flow, indicating that the centre of pressure moves towards the mid-chord as the suction surface becomes aerated. The lifting-line model, in concert with (3.4), was used to estimate C_M, plotted as dashed lines. The relatively good agreement suggests that the combined reductions in lift and shift in the centre of pressure together adequately describe the trend in C_M.

drag predicted by the lifting-line model is caused by the previously noted decrease in lift, and suggests that those drag components not captured by the lifting-line model, namely profile and spray drag, are substantially increased by the formation of a ventilated cavity.

The yawing moment coefficient, C_M, measured about mid-chord, is shown in figure 14. The FW data follow a roughly linear trend, except near the stall boundary, where a reduction in the yawing moment indicates impending stall and an accompanying shift in the centre of pressure towards the mid-chord. The FV data exhibit a significant reduction in C_M, compared with the wetted data. This is partly due to the reduction in C_L shown in figure 12, and is compounded by the movement of the centre of pressure towards the mid-chord, resulting in a sub-linear trend in C_M with respect to changing α. The lifting-line code was used to approximate the yawing moment, also shown in figure 14. The dimensionless location of the centre of pressure for FW sections is estimated to be $e_{FW} = x_{cp}/c = 1/4$, where x_{cp} is the location of the centre of pressure forward of mid-chord. For supercavitating sections, $e_{SC} = 3/16$ (Akcabay & Young 2014). A sigmoid function was used to smoothly interpolate between the bounding values as a function of sectional cavity length,

$$e(L_c/c) = \frac{1}{2}\left\{ e_{FW}\left[1 - \tanh\left(\frac{L_c/c - 0.5}{0.25}\right)\right] + e_{SC}\left[1 + \tanh\left(\frac{L_c/c - 0.5}{0.25}\right)\right]\right\}. \quad (3.4)$$

The effect of Froude number is also of interest. In figure 15, C_L is plotted as a function of α at values of Fn_h between 0.5 and 3.5, forming surfaces representing the FW and FV regimes. Two-dimensional plots of hydrodynamic load coefficients with varying Froude number may be found in figures 31–33 in appendix A. In the FW regime, the C_L contours are parallel to the Fn_h axis for $Fn_h > 1$, indicating that C_L is speed-dependent only at very low speeds. For $Fn_h \leqslant 1$, the Reynolds numbers are low ($Re_c \leqslant 5 \times 10^5$), resulting in leading edge laminar separation, which in turn

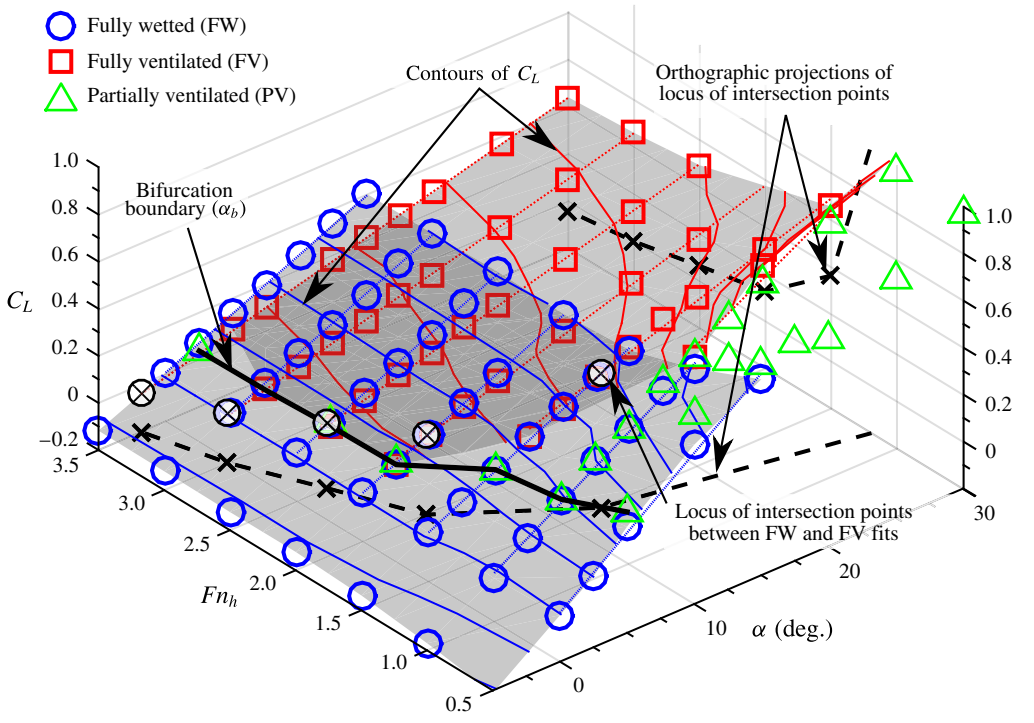

FIGURE 15. (Colour online) The C_L surface as a function of α and Fn_h for $AR_h = 1$. Contours of constant C_L are shown as solid lines in the FW and FV regimes (the PV surface and contours are omitted for clarity). It is a strong function of Fn_h in the FV regime, where for a fixed α, C_L decreases as Fn_h increases. At low speeds ($Fn_h \leqslant 1$), laminar separation occurs at the accompanying low Reynolds numbers ($Re_c \leqslant 5 \times 10^5$), causing an increase in C_L in the FW regimes. Affine fits of C_L as a function of α are shown as dotted lines at each Fn_h, with the intersection between the FW and FV fits indicated by cross-hatched circles. The dashed lines are orthographic projections of the locus of intersection points onto the α–Fn_h plane and the Fn_h–C_L plane. A heavy solid line indicates the locus of bifurcation angles (α_b), forming a bifurcation boundary, below which only FW flow was observed.

causes a characteristic increase in lift (Breslin & Skalak 1959). In the fully ventilated regime, lift monotonically decreases with increasing Froude number at a fixed angle of attack, made apparent by the curvature of the C_L contours in the FV regime. This behaviour is due in part to longer cavity lengths at each section along the span (caused by the reduction in sectional σ_c at high Froude numbers), which lead to reduced lift coefficients (see figure 2*b*). Additionally, longer sectional cavity lengths present a smaller amount of apparent camber to the flow, causing further reduction in the sectional values of $C_{l_{2D}}$. Affine curve fits through the C_L values in the FW and FV flow regimes with respect to α are shown as dotted lines. Cross-hatched circular markers indicate the intersection between the FW and FV affine data fits at each respective value of Fn_h. The dependence of C_L upon Fn_h in the FV regime leads to intersection points at increasingly large angles of attack as the Froude number is decreased. Orthographic projections of this locus are made onto the α–Fn_h and

Fn_h–C_L planes and are shown as black dashed lines in figure 15. It should also be noted that, while not shown in figure 15 to avoid overcrowding, the nonlinear lifting line correctly represents the qualitative behaviour of C_L with changing Fn_h. The model results do not yield a good qualitative match to experimental measurements across the entire Fn_h domain – thought to be because effects such as the apparent camber are not modelled – but the decrease in C_L with increasing Fn_h in the FV regime is present.

Partially ventilated data are also present in figure 15; however, the C_L contours and surface fit are omitted for the PV regime to avoid overcrowding. It should be recalled that the bifurcation angle (α_b) was shown in figure 12 to be $\alpha_b \approx 2.5^\circ$ at $Fn_h = 2.5$ and $AR_h = 1.0$. With the inclusion of PV data, the meaning of the bifurcation angle may be further clarified. The bifurcation angle is defined for a given Froude number as the angle below which FW flow was the sole flow regime observed during experiments. In figure 15, the bifurcation angles form a 'bifurcation boundary', shown as a solid black line. The bifurcation boundary takes on a value of $\alpha_b \approx 2.5^\circ$ at $Fn_h \geqslant 2$, and increases along the α-axis with decreasing values of Fn_h for $Fn_h < 2$. In the neighbourhood of α_b, values of C_L in the FW, FV and (where applicable) PV regimes are nearly coincident. This observation suggests that the suction-surface pressures of the wetted flow near α_b are only mildly sub-atmospheric, so that ventilation formation does not materially affect the magnitude of suction-surface pressures. Reinforcing this hypothesis, the intersection of the affine curve fits approximates the bifurcation angle (α_b) at each value of Fn_h.

The bifurcation is so named because above α_b, other alternate flow regimes become stable, forming characteristic branches in the plots of stable hydrodynamic load coefficients. The other critical angle is the stall angle (α_s), above which FW flow was never observed, and so named because large eddies were observed in the wake of the foil at $\alpha > \alpha_s$, indicating massive flow separation. For the present foil and for $AR_h = 1$, stall was observed at approximately $\alpha_s = 14^\circ$–15° for all values of Fn_h tested. Smaller values of AR_h were observed to increase the stall angle slightly (see appendix A). A range of bi-stable flow conditions exists for $\alpha_b \leqslant \alpha \leqslant \alpha_s$ in figures 12–14, as well as in the overlap of the FW and FV surfaces in figure 15. Under such conditions, stable FW flow overlaps with PV or FV flow, and the flow can take on alternate stable configurations.

3.4. *Stability regions of the three stable flow regimes*

The FW, FV and PV flow regimes are mapped as functions of α and Fn_h for an immersed aspect ratio of $AR_h = 1.0$ in figure 16. The experimentally observed flow regimes reveal three distinct stability regions (indicated by solid shading), which overlap in zones 1, 2 and 3 (indicated by hatching). The bifurcation boundary shown in figure 15 is drawn as a heavy solid line in figure 16. Below and to the left of this boundary, FW flow alone was observed. It should be noted that $\alpha = 2.5^\circ$ was the smallest non-zero angle tested; the verticality of the bifurcation boundary is therefore probably a result of the testing resolution, and FV or PV flow might be attainable at $\alpha < 2.5^\circ$ for large Fn_h. The rightmost extent of the FW regime is indicated by the vertical stall boundary, formed by the collection of stall angles (α_s), which appears to be independent of Fn_h. The regions of overlap indicate bi-stable flow conditions, where mutually stable flow regimes coincide. For example, the bi-stable range of α shown in figures 12–14 corresponds to the overlap of FW and FV regions (in zone 1) along a horizontal cut through figure 16 at $Fn_h = 2.5$. In addition to overlap with

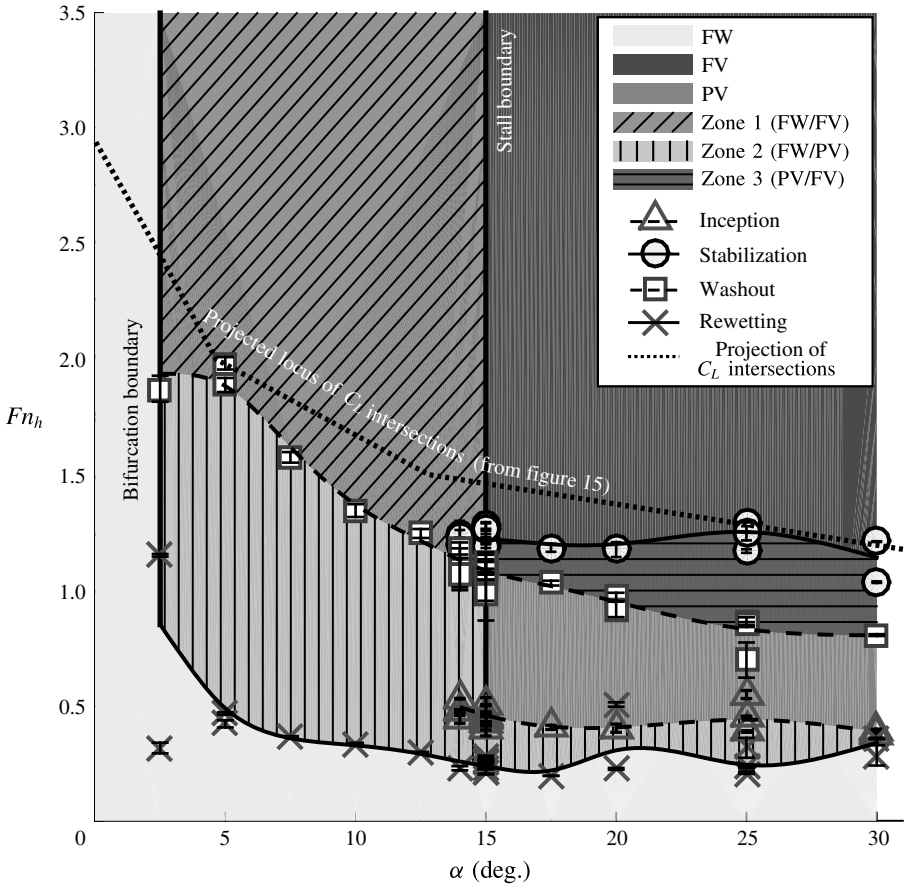

FIGURE 16. Steady flow regime map for the hydrofoil as a function of α and Fn_h at a fixed aspect ratio of $AR_h = 1.0$. Shaded regions indicate experimentally observed stable flow regimes. Overlapping zones (numbered 1 through 3) are denoted by hatching, and are indicative of bi-stable flow. Symbols indicate experimentally observed regime boundaries, through which are fitted approximate curves. Uncertainty bars indicate the range in which ventilation transition events were observed to occur. Heavy solid lines on the left and right indicate the bifurcation boundary (the locus of α_b, as shown in figure 15) and the stall boundary (the locus of maximum observed stall angles, $\alpha_s \approx 15°$). The heavy dotted line is an orthographic projection of the locus of points marking the approximate intersection of C_L in the FW and FV flow regimes, also shown in figure 15.

respect to α, the three regimes overlap their neighbours in the Fn_h direction as well, which has not previously been noted. The edges of the stability regions are populated with symbols, which denote experimentally observed processes that cause transition from one flow regime to another. These ventilation transition mechanisms will be described in § 4. The locus of intersection points between fitted values of C_L in the FW and FV regimes (from figure 15) has been orthographically projected onto the α–Fn_h plane, shown by the bold dotted line. The locus projection mimics the shape of the lower extent of FV flow, suggesting that near the boundary between the FV regime and the other two regimes, the lift coefficients in the three flow regimes do not strongly differ from one another.

3.5. *Discussion: steady flow regimes*

This section develops a few important ideas. First, it establishes that spanwise variation in the cavity length leads to re-entrant jet velocities that are well approximated by (3.2*a*) and (3.2*b*). Second, it verifies that the linearized slope of the cavity closure line ($\bar{\Phi}$) is a suitable metric for predicting the presence of a destabilizing re-entrant jet. It should be recalled that the spanwise non-uniformities of the cavity are caused by combined 3D effects, gravity and nonlinear section forces, the gross effects of which are represented quite well by the nonlinear lifting-line model presented in § 1.2.2.

The division between the three flow regimes has been made on the basis of the stability of the flow. It should be noted that unsteadiness should not be confused with instability, as some stable flows (e.g. PV flow) may be inherently unsteady, even while locally or globally stable. A limitation applies to the flow-regime criteria developed in § 3.2. Callenaere *et al.* (2001) and Franc & Michel (2006) point out that thin cavities (which occur at small attack angles) cause correspondingly thin re-entrant jets to develop. These jets are more severely affected by wall friction than are thicker jets; the thinness of the cavities means that the jets often collide with – and become re-entrained in – the external flow. Thus, for small angles of attack ($\alpha \lesssim 5^\circ$), the thin jet is not sufficient to perturb the flow away from its locally stable configuration, so the $\bar{\Phi} = 45^\circ$ condition is not expected to reflect the stability of the flow at such small attack angles. However, when small cavities with closure angles of $\bar{\Phi} \approx 45^\circ$ were subjected to external perturbations (air injections, small ripples, spray sheet, etc.), the flow often underwent a transition to PV flow, from which FV flow did not resume. At such small attack angles, $\bar{\Phi} = 45^\circ$ is retained as the division between flow regimes – not because it necessarily signals instability caused by a re-entrant jet, but because it is a convenient and repeatable visual distinction which belies a tenuously stable flow configuration.

The establishment of three ventilated flow regimes is important for two reasons. First, it standardizes the definitions under which ventilated flow may be discussed and results disseminated. Previous studies have used disparate terminology. Second, it lays a groundwork from which to begin investigating the mechanisms of transition between ventilation regimes. Finally, a systematic method of characterizing the flow regimes is also necessary for establishing scaling relations for stability boundaries, more of which will be discussed in § 4.2.1.

The overlapping zones in figure 16 are of interest because they represent bi-stable conditions, where the flow may take on either one of the locally stable regimes. Factors governing the regime of a given flow include hysteretic effects with movement through the parametric map (such as during flow acceleration and deceleration) or external perturbations to the flow. Transition between two locally stable regimes is possible wherever the stability regions of those respective regimes abut or overlap one another. Overlaps along the Fn_h-axis are particularly interesting, and merit further investigation. The stability boundaries were measured in accelerating and decelerating conditions (described further in § 4), so there is the possibility that some inertial and wake-memory effects are present. All efforts were made, however, to minimize such effects when populating the boundaries of figure 16 (see appendix B), so the overlaps are thought to be indicators of true bi-stable flow conditions, and not just transient effects.

4. Results: ventilation formation and elimination

Ventilation transition mechanisms collectively describe the processes by which the flow moves between stable regimes, either by crossing stability boundaries (the

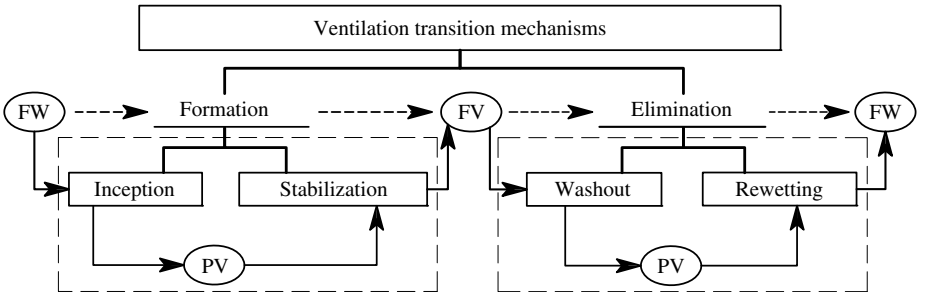

FIGURE 17. Process chart showing the hierarchy of ventilation transition mechanisms. The first level distinguishes the overall direction of transition. The second level identifies the individual stages of transition between the three steady flow regimes.

edges of regions in figure 16) or by moving between two mutually stable regimes (in zones 1, 2 or 3 of figure 16). A hierarchy of ventilation transition mechanisms is shown in figure 17, illustrating how each mechanism links the steady flow regimes defined in § 3.2. The first distinction between transition mechanisms is made on the basis of the overall direction of the transition, dividing ventilation transition into 'formation' and 'elimination' mechanisms. Ventilation formation mechanisms are described in § 4.1 and elimination mechanisms are discussed in § 4.2. Movies of each of the processes are included in the online supplementary material available at http://dx.doi.org/10.1017/jfm.2016.373.

4.1. *Ventilation formation*

Formation mechanisms promote the growth and stability of a cavity, causing the flow to transition from an FW or PV regime to a PV or FV regime respectively (see figure 17). Formation mechanisms can be further decomposed into two sequential stages, as follows.

Inception is the transition from FW flow to PV flow, which marks the first stage in the formation of a ventilated cavity. The first visual evidence of persistent air entrainment is sufficient to classify inception. Triangular symbols along the upper boundary of the FW region for $\alpha \geqslant 14^\circ$ in figure 16 indicate spontaneous ventilation inception (§ 4.1.1). Ventilation inception may also occur in zones 1 and 2 of figure 16, where the FW regime overlaps the FV and PV regimes respectively (described in § 4.1.2).

Stabilization is the transition from PV flow to FV flow, which completes ventilation formation. Stabilization is said to occur when the flow satisfies the criteria established for FV flow in § 3.2. Circles along the upper boundary of the PV region in figure 16 denote spontaneous stabilization events. Stabilization also immediately follows inception in zone 1 of figure 16. Under suitable conditions, stabilization can occur in zone 3 as well.

The two stages of ventilation formation can occur on multiple time scales and through different physical processes. Spontaneous formation mechanisms occur by self-initiated features of the flow. Perturbation-induced formation mechanisms, on the other hand, occur when some external influence perturbs the flow away from its locally stable state.

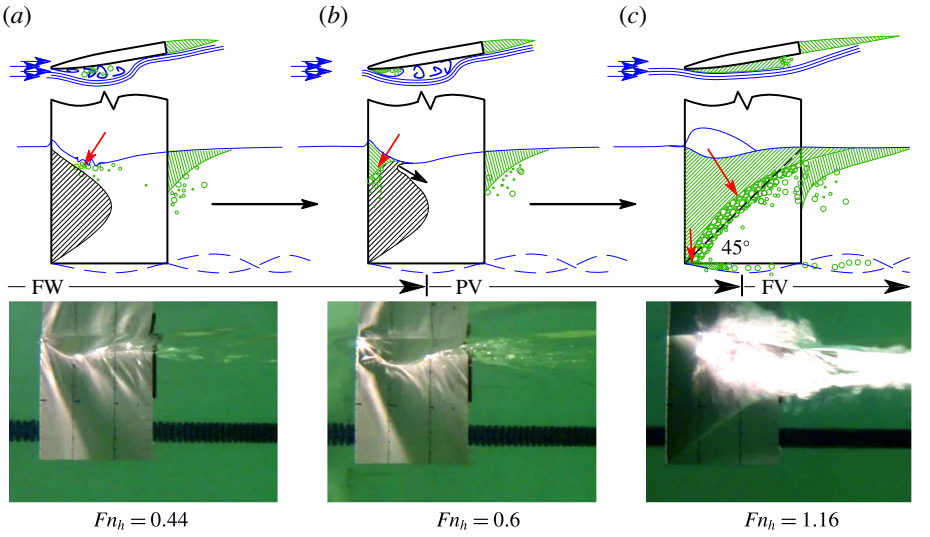

FIGURE 18. (Colour online) Spontaneous stall-induced ventilation formation occurring at $\alpha = 15^\circ \approx \alpha_s$, $AR_h = 1$. Here, Fn_h is given at the instant of each photograph. Blue lines denote streamlines, green lines and hatching indicate entrained air, black hatching indicates boundary layer separation and red arrows indicate air-ingress paths. A movie of this process is also included in the online supplementary material (movie 1).

4.1.1. *Spontaneous formation*

Spontaneous formation mechanisms were examined by accelerating the towing carriage (constituting an upward vertical trajectory through the space of figure 16). Inception and stabilization were recorded to form the respective boundaries.

Stall-induced formation occurs when the angle of attack is set at or above the stall angle ($\alpha \geqslant \alpha_s$). An example of the stall-induced ventilation formation process is depicted in figure 18, along with experimental photos of the hydrofoil suction surface. The flow begins in the FW regime. A large leading edge vortex creates a stagnant region of wetted separation, indicated by black hatching. In (*a*), the low pressures on the hydrofoil surface create a steep depression of the free surface, forcing proximity between the free surface (an air source) and the separated flow (ventilation-prone flow). At the same time, small vortical disturbances develop near the toe of the free-surface depression. Such vorticity development was noted in the waves generated by an unyawed surface-piercing hydrofoil by Pogozelski, Katz & Huang (1997). The vortical structures at the free surface temporarily breach the surface seal, admitting air into the separated flow. If enough air is admitted, then it becomes stably entrained, constituting inception, shown in (*b*). After inception, the flow is classified as PV. As the flow velocity increases, the suction-side dynamic pressure negates the hydrostatic pressure to increasing depths and the sectional values of σ_c decrease, causing the cavity to grow in both length and depth. As the cavity grows, it modifies the local chordwise pressure gradients, causing the separated flow to propagate ahead of the cavity (Tassin-Leger & Ceccio 1998), creating a moving front of ventilation-prone flow. The instant when the cavity meets the conditions for FV flow given in § 3.2 ($D = h$ and $\bar{\Phi} < 45^\circ$) is shown in (*c*). This constitutes stabilization, beyond which point the flow is classified as FV. Stall-induced formation is a quasi-steady process, wherein the flow takes on an evolving state of equilibrium as the speed, and hence

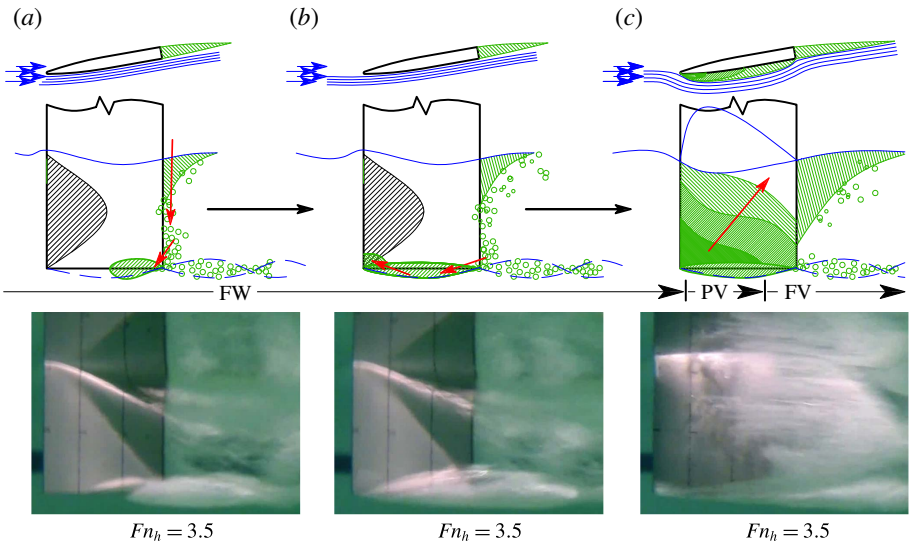

FIGURE 19. (Colour online) Tip vortex ventilation formation occurring at angles near stall, $\alpha = 15° \approx \alpha_s$, $AR_h = 1$. Here, Fn_h is given at the instant of each photograph. Time is increasing from left to right at a constant Froude number for the case shown. The process may be seen in movie 2 of the online supplementary material.

the pressure distribution, changes. As a result, cavity formation takes place on a time scale governed by the acceleration of the hydrofoil.

Another case of spontaneous ventilation formation occurs when air enters the tip vortex at a downstream location and is transported upstream through the aerated vortex core. 'Tip vortex inception' was observed by Breslin & Skalak (1959) and Swales *et al.* (1974) only at large angles of attack and small immersion depths (described in § 1.1). In the present experiments, air entered the tip vortex through the bubbly wake of the blunt trailing edge of the foil. A process sketch and experimental photos are shown in figure 19. The flow begins in the FW regime, with a base-vented cavity attached to the blunt trailing edge. Eddies in the wake draw air bubbles into the low-pressure core of the tip vortex, where they coalesce into an aerated vortex core, shown in (*a*). The coalesced bubble migrates up the low-pressure core towards the leading edge of the foil, where it encounters a favourable pressure gradient, as shown in (*b*). In (*c*), the air reaches the region of separated flow and expands rapidly upwards and towards the foil trailing edge. Fully ventilated flow is attained in a fraction of a second, with no appreciable dwell in the PV regime. Tip-vortex-induced formation occurred only at $AR_h = 1.0$, at yaw angles very near the stall boundary ($\alpha \approx 15°$), and at $Fn_h \approx 3.5$.

Figure 20 depicts a surface-flow visualization at $Fn_h = 2.5$, $\alpha = 14°$, $AR_h = 1.0$, corresponding to a location near the upper right corner of the FW stability region (in zone 1) in figure 16. A large separation bubble is clearly visible, indicated by the forward-swept paint streaks and black dashed outline. The separation bubble is conducive to both stall-induced formation and tip-vortex-induced formation. In the former case, air ingress occurs through disturbances in the thin layer of liquid between the separation bubble and the free surface, indicated by the free-surface profile and superimposed arrow in (*a*). In the latter case, air ingress occurs when a

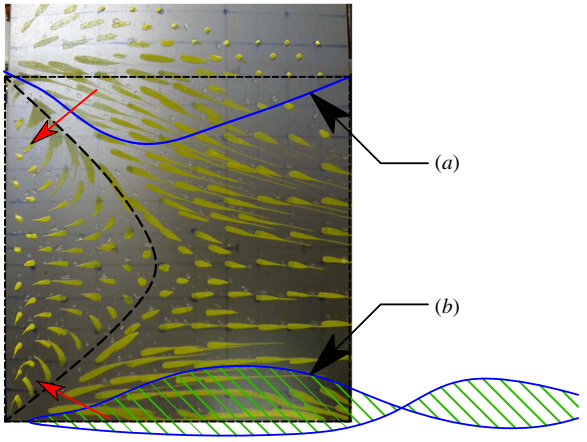

FIGURE 20. (Colour online) Surface-flow visualization for $\alpha = 14°$, $Fn_h = 2.5$, $AR_h = 1.0$, showing two possible mechanisms of ventilation inception (the first stage of ventilation formation). Red arrows indicate the respective ingress paths of air. (*a*) The free-surface profile immediately preceding spontaneous stall-induced inception. (*b*) The aerated tip vortex immediately preceding tip-vortex-induced inception.

tip vortex develops of sufficient strength to transport air upstream to the separation bubble, shown in (*b*). Both stall-induced formation and tip-vortex-induced formation result when naturally occurring air paths reach the regions of flow separation.

The time histories of instantaneous lift, drag and moment coefficients of the two trials pictured in figures 18 and 19 are plotted against the instantaneous Froude number in figure 21. It should be noted that at small Fn_h, the denominators of (3.3) vanish, and fluid inertial forces are large relative to the quasi-steady (velocity-dependent) load. As a result, C_L, C_D and C_M may not be representative of steady-state results for $Fn_h < 1$. The grey and black traces describe two separate runs, each comprising an acceleration and deceleration cycle. Dashed arrows indicate the direction of the traces with increasing time. Symbols indicate steady-state force and moment coefficients. It should be noted that the steady-state data shown are projections of the same points shown in figures 12–15, plotted for a fixed α at different values of Fn_h. The lettered markers indicate the corresponding panels in figures 18 and 19. The trace corresponding to stall-induced formation (solid black line in figure 21) follows the PV and FV markers during acceleration and deceleration, with the forces passing gradually through the inception and stabilization events at increasing values of Fn_h. In the case of tip-vortex-induced formation (dashed grey line in figure 21), the loads pass through the FW points during the acceleration phase. At $Fn_h = 3.5$, inception and stabilization occur rapidly at a constant speed, indicated by a precipitous drop in C_L and C_M. During deceleration, the measured forces and moment follow the FV and PV points, overlapping with the deceleration section of the stall-induced formation case.

4.1.2. *Perturbation-induced formation*

In addition to the spontaneous formation processes observed at the boundaries of the stability regions, ventilation formation may be triggered by an external perturbation to an otherwise steady flow. When the parameters of a flow are inside one of the overlapping zones in figure 16, a suitable perturbation will destabilize the locally

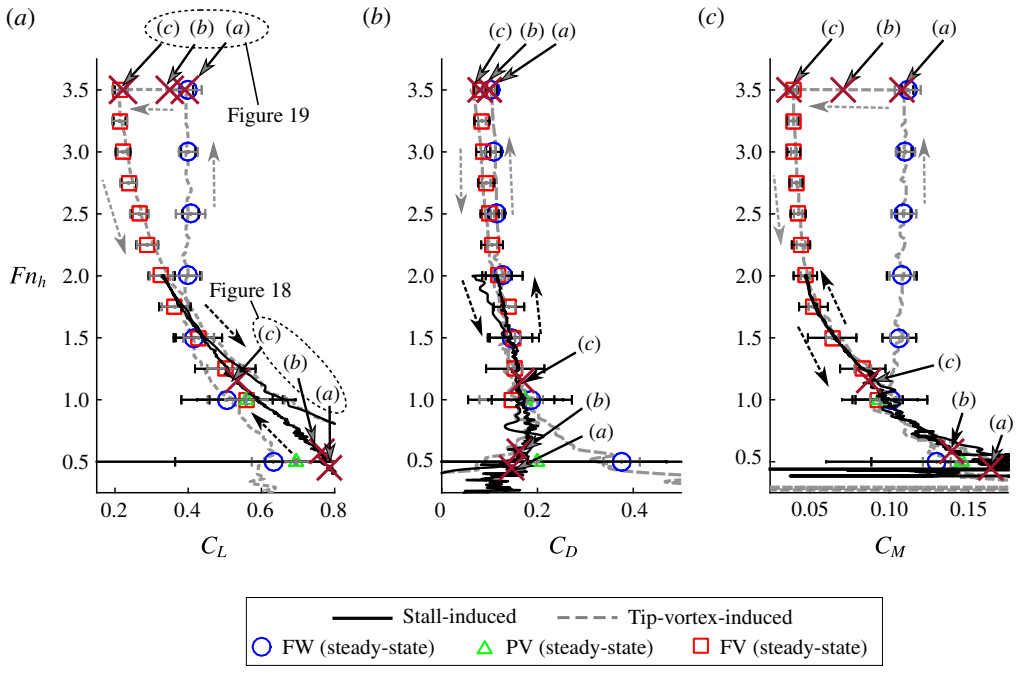

FIGURE 21. (Colour online) Time histories of lift, drag and moment coefficients for stall-induced (as depicted in figure 18) and tip-vortex-induced (as depicted in figure 19) ventilation formation at $\alpha = 15°$, $AR_h = 1$. Dashed arrows indicate the acceleration and deceleration stages of the runs. Steady-state force/moment coefficients for all runs at $\alpha = 15°$ are plotted as open symbols, with measurement uncertainties and standard deviations indicated respectively by grey and black horizontal bars.

stable flow state and initiate a jump to a lower-energy state (FW to FV via inception and stabilization in zone 1, FW to PV via inception in zone 2, and PV to FV via stabilization in zone 3).

Figure 22 shows a sketch of a perturbation-induced ventilation formation process that would occur in zone 1. In (*a*), the flow is FW. Compared with the case of stall-induced formation, the leading edge separation bubble is small and the large Froude number means that the free surface is not so steeply deformed, so the free surface never approaches the boundary of flow separation. As a result, a thin layer of attached flow exists just below the free surface (indicated by a dashed line), sealing the ventilation-prone flow from the ingress of air. In (*b*), a high-pressure jet of air is injected at the junction of the leading edge and the free surface, introducing vorticity and bubbles into the flow at the free surface to break the surface seal. In (*c*), a small cavity is entrained and grows rapidly from the point of inception towards the immersed trailing edge until it reaches the lower-energy FV state. Entrainment and stabilization are nearly concurrent in this case, with little to no dwell in the PV regime. Fully ventilated flow can develop in approximately 1/10th of a second following perturbation.

Figure 23 shows the surface-flow pattern at $\alpha = 10°$, $Fn_h = 2.5$, $AR_h = 1.0$. The small yaw angle creates a short leading edge separation bubble, where flow reversal has swept several of the forwardmost columns of paint dots towards the leading edge. The free surface in the FW regime is superimposed as line (*a*). When air injection is

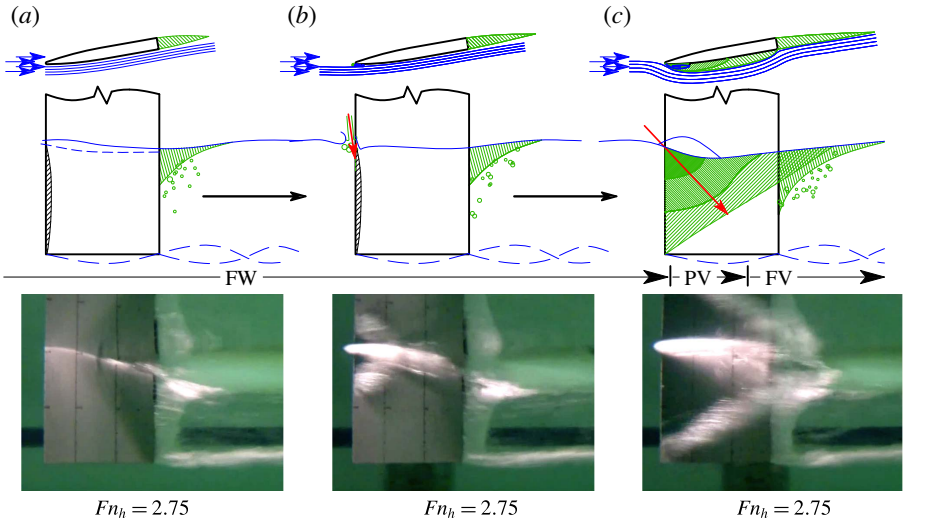

FIGURE 22. (Colour online) Perturbed ventilation formation occurring at sub-stall, $\alpha = 10^\circ < \alpha_s$, $AR_h = 1$, $Fn_h = 2.75$ (inside zone 1 of figure 16). Blue lines denote streamlines, green lines and hatching indicate entrained air, black hatching indicates boundary layer separation, the blue dashed line indicates the free-surface seal and red arrows indicate air-ingress paths. The process may be seen in movie 3 of the online supplementary material.

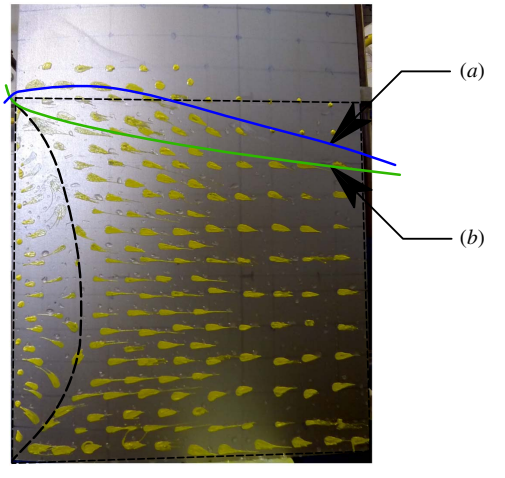

FIGURE 23. (Colour online) Surface-flow visualization for $\alpha = 10^\circ$, $Fn_h = 2.5$, $AR_h = 1.0$. The dashed line depicts the leading edge separation bubble caused by thin-airfoil stall. (*a*) The free-surface profile prior to ventilation inception and (*b*) the air-filled depression created by the air-jet perturbation.

initiated, the depression of the free surface permits air to enter the small bubble and expand, shown by line (*b*). Again, experimental observations support the hypothesis that inception occurs when an air supply is made available to ventilation-prone flow.

Time histories of the lift, drag and moment coefficients of the process pictured in figure 22 are plotted against the instantaneous Froude number in figure 24.

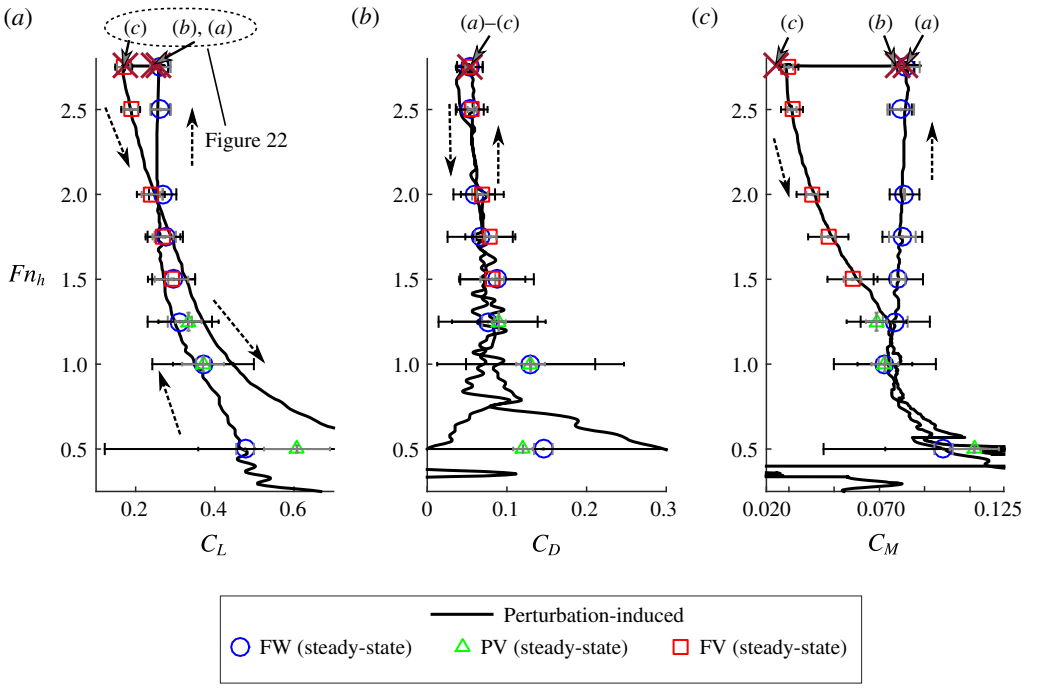

FIGURE 24. (Colour online) Time histories of lift, drag and moment coefficients for perturbation-induced ventilation formation at $\alpha = 10°$, $AR_h = 1$. The lettered markers correspond to the panels in figure 22. Dashed arrows indicate the acceleration and deceleration stages. Steady-state force/moment coefficients for all runs at $\alpha = 10°$ are plotted as open symbols, with measurement uncertainties and standard deviations indicated respectively by grey and black horizontal bars.

The resulting hysteresis loop is similar to that created by tip-vortex-induced formation in the sense that large changes in hydrodynamic loading occur on a short time scale, and at otherwise steady flow conditions.

4.1.3. *Discussion: ventilation formation*

To summarize, ventilation inception is the first stage of formation, and it requires that air enters low-pressure and locally separated flow. Spontaneous inception occurs when some self-induced process of the flow admits air from a natural source. Perturbation-induced inception requires that an external source of air be provided, an example being the air jet used in the present study. Air can only become stably entrained where low pressure permits its ingress and separated flow permits its residence. It is hypothesized that the entrained air modifies the local pressure gradients, inducing further flow separation, as observed in vaporous cavitating flows by Tassin-Leger & Ceccio (1998). If an air supply is continuously available, this will result in a cavity that expands by propagating flow separation ahead of it, and then occupying the newly separated flow in a continuous evolution. Equilibrium will be reached when the increasing hydrostatic pressures – and not the extent of flow separation – arrests the growth of the cavity. It is thought that this evolution of separation and propagation occurs very suddenly for short-time-scale formation processes such as tip-vortex-induced ventilation and perturbation-induced ventilation,

and very gradually for stall-induced formation. Such a hypothesis requires further validation, but, if verified, it would be consistent with the idea that destabilization of a steady FW flow leads to the formation of an FV flow as a second stable flow state. The second stage of formation, stabilization, occurs when the cavity grows to satisfy the conditions for FV flow in § 3.2. Stall-induced ventilation formation is consistent with the description by Wetzel (1957) of 'creeping' ventilation, occurring at post-stall yaw angles. Both tip-vortex-induced ventilation formation and perturbation-induced ventilation formation are consistent with Wetzel's description of 'flash ventilation', occurring at sub-stall yaw angles.

At high speeds, vaporous cavitation is often a precursor to atmospheric ventilation (Waid 1968; Rothblum *et al.* 1969; Hecker & Ober 1974). At the speeds achieved in the towing tank, however, the range of vaporous cavitation numbers given in table 2 is much too high ($\sigma_v \geqslant 5.4$) to induce vaporization. Thus, the results presented here do not account for the influence of vaporous cavitation. The formation mechanism of 'tail ventilation' caused by Taylor instabilities (Rothblum *et al.* 1969; Swales *et al.* 1974) was never observed in the present experiments. One possible explanation lies in the section shape of the model. Previous studies have used models with sharp trailing edges and convex curvature on the afterbodies, while the present model has a blunt trailing edge with a rectangular afterbody. As a result, the adverse pressure gradient and wetted flow separation observed at the trailing edge of those models were not present on the current model, meaning that air ingress must occur near the leading edge in the present experiments. Moreover, base ventilation occurs in the present experiments where it was not observed in previous ones, providing an alternate air path (e.g. the location of vortex aeration in tip-vortex-induced formation) to those noted in the literature.

Previous studies have also indicated an effect of Weber number and Reynolds number on ventilation formation boundaries, as most were conducted with small-scale models at lower Weber numbers and Reynolds numbers than the present tests. These effects influence the rupture of the free-surface seal and boundary layer separation respectively (Wetzel 1957; Breslin & Skalak 1959). However, the data of Wetzel (1957) showed that the effect of the Weber number was significant only when $We \lesssim 250$, so surface tension becomes negligible at the present model scale, where $We \gtrsim 10^4$. Moreover, the separation bubble indicated by the surface-flow visualizations is not thought to be a strong function of the Reynolds number. The works of Gault (1957), Chang (1960), Chang (1961) and Hecker & Ober (1974) indicate that, for the sharp-nosed geometry used, separation is of the thin-airfoil type, and is primarily a function of the angle of attack. If a streamlined foil section were to be used, the size of the separation bubble would probably be more susceptible to Reynolds number effects.

4.2. *Ventilation elimination*

Elimination encompasses processes that detract from the size or stability of a ventilated cavity. They describe the movement from an FV or PV regime towards a PV or FW regime respectively (see figure 17). As with formation mechanisms, elimination mechanisms can be broken down into two stages, given as follows.

Washout marks the transition from FV flow to PV flow. Washout is said to occur when the criteria for fully ventilated flow given in § 3.2 are no longer satisfied. This typically corresponds to a large-scale shedding of the cavity, after which the cavity topology fluctuates visibly. Squares along the lower edge of the FV region in figure 16 denote the washout event.

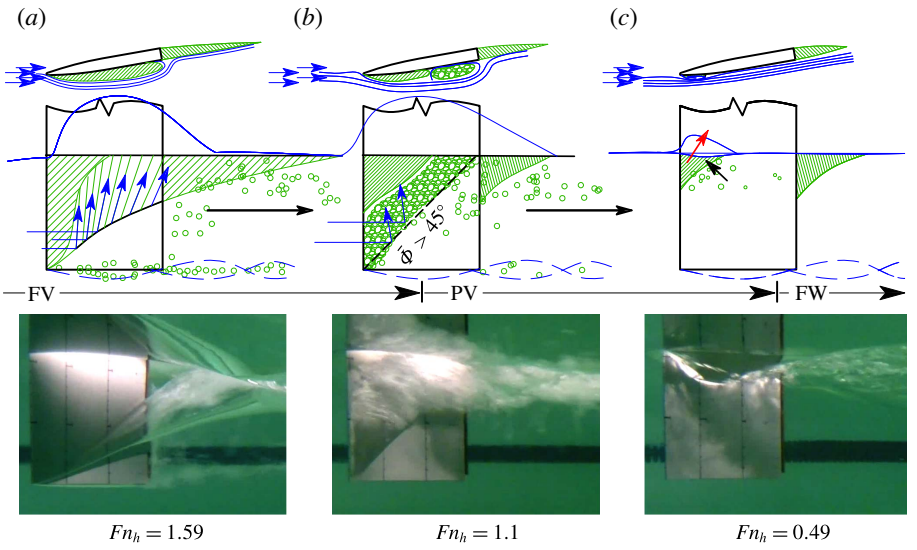

FIGURE 25. (Colour online) Ventilation elimination process. Flow speed is decreasing from (*a*) to (*c*). Here, Fn_h is given at the instant of each photograph. Blue lines denote streamlines, green lines and hatching indicate entrained air, and red arrows indicate air egress paths. The process may be seen in movie 4 of the online supplementary material.

Rewetting marks the termination of air entrainment. It was observed that air was frequently ejected from the flow by laminar/turbulent reattachment of the flow at low speeds and angles of attack. It is said to occur when there ceases to be any visual evidence of air entrainment on the suction or pressure surfaces; there may still be bubbly flow entrained in the separated wake of the blunt trailing edge. Typically, the connection between the cavity and the free surface is terminated as the shallowly immersed sections experience flow reattachment. Isolated pockets of air cling to the leading edge of the hydrofoil until widespread reattachment of the flow sweeps the bubbles away. The 'X' symbols at the lower edge of the PV region in figure 16 indicate observed rewetting events.

Ventilation elimination was investigated by starting from an FV state and decelerating the hydrofoil, describing a downward trajectory in figure 16, during which washout and rewetting were recorded to form the stability boundaries. A sketch of ventilation elimination is shown in figure 25. The flow begins in an FV condition. In (*a*), a re-entrant jet develops on the deeply immersed hydrofoil section (shown by blue arrows). The cavity closure angle is shallow ($\bar{\Phi} < 45°$), so the jet flow does not impinge on the upstream flow. As the hydrofoil decelerates, the cavity remains attached to the immersed tip, but reduces in its length, causing the angle of the cavity closure line to increase. In (*b*), the mean cavity closure angle just exceeds 45°, imparting an upstream velocity component to the re-entrant jet, per (3.2). The jet pinches off a large portion of the cavity, causing it to be shed downstream (washout), leaving the flow in a PV state, from which FV flow does not resume. As the flow velocities decrease further in (*c*), the partial cavity is confined to a shrinking region near the leading edge of the foil and the free surface. Eventually, the remaining air is ejected by laminar/turbulent reattachment of the flow, constituting rewetting and the return to the FW regime.

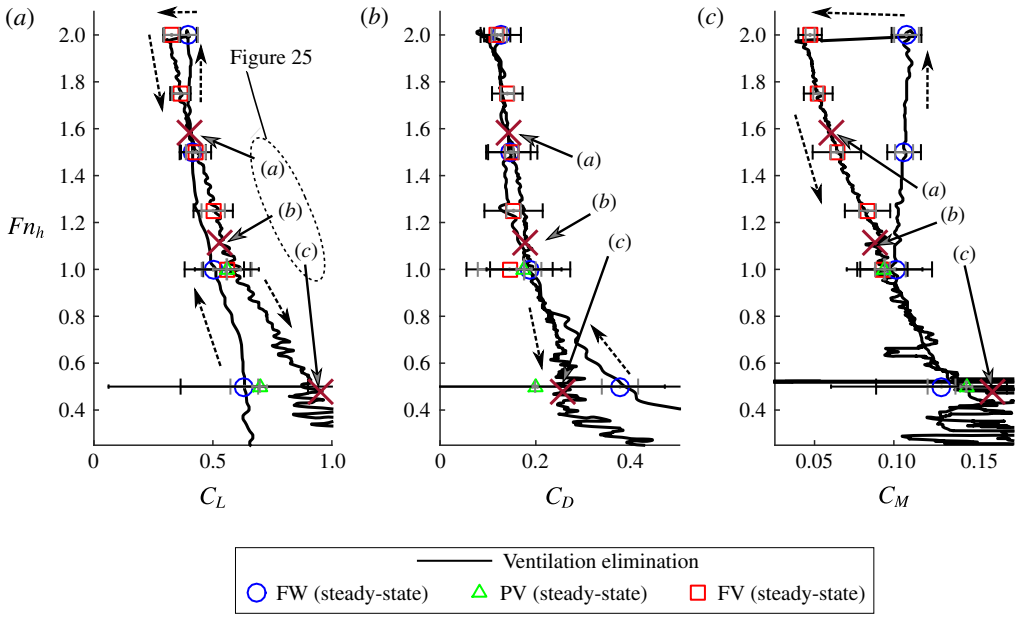

FIGURE 26. (Colour online) Time histories of lift, drag and moment coefficients for the ventilation elimination process at $\alpha = 15°$, $AR_h = 1$. Dashed arrows indicate the acceleration and deceleration stages. The lettered markers correspond to the panels in figure 25. Perturbation-induced formation was used to achieve FV flow prior to deceleration. Steady-state force/moment coefficients for all runs at $\alpha = 15°$ are plotted as open symbols, with measurement uncertainties and standard deviations indicated respectively by grey and black horizontal bars.

The time history of lift, drag and yawing moment coefficients can be observed during the deceleration stages of figure 26. Following ventilation formation (which occurred via external perturbation for the case shown), the instantaneous forces and moments pass through the steady-state FV points, but return to the PV or FW regime at very small values of Fn_h. The yawing moment coefficient most clearly shows the measured C_M returning to the FW and/or PV values. It should be noted that when $Fn_h < 0.5$, the denominators of (3.3) are vanishingly small, so any noise in the signal is amplified. For this reason, the return of the hydrodynamic forces and moments to the FW values at low speeds is not obvious in the time histories shown. It should also be noted that in the neighbourhood of washout, indicated by marker (*b*), the hydrodynamic force/moment coefficients in the FW, PV and FV regimes are nearly coincident; this corroborates the observations from figure 15 that the intersection of C_L values between the FW and FV regimes follows the lower boundary of the FV flow regime.

4.2.1. *Scaling of washout stage*

The experimentally observed washout boundaries from the present experiment are plotted as open symbols in figure 27 as functions of the instantaneous lift coefficient C_L and Fn_h for the three immersed aspect ratios ($AR_h = 0.5$, 1, 1.5). The plotted data denote the combination of Fn_h and C_L at the moment that washout was visually observed, e.g. in panel (*b*) of figure 25 and marker (*b*) in figure 26. Data from Breslin & Skalak (1959) for hydrofoils with circular-arc and cambered NACA sections at four

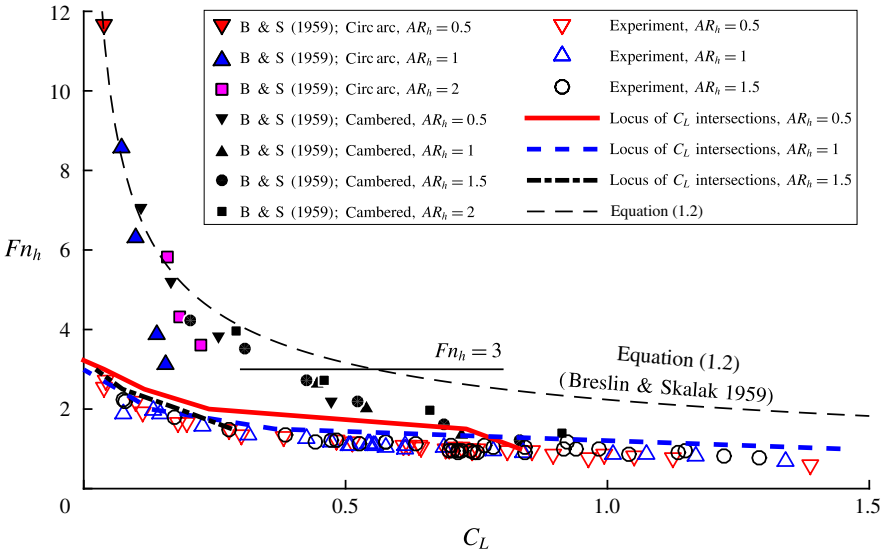

FIGURE 27. (Colour online) Scaled washout boundary in C_L, Fn_h space. Data from the present experiments at three immersed aspect ratios, plotted as open symbols, and the experimentally observed boundary from Breslin & Skalak (1959) for cambered and circular-arc hydrofoils at four immersed aspect ratios, plotted as filled symbols, are shown. Equation (1.2) overpredicts the washout Froude numbers from the present experiments. The projected loci of lift-intersection points closely match the washout boundaries, suggesting that the lift coefficient is similar between the three flow regimes at washout.

immersed aspect ratios ($AR_h = 0.5, 1, 1.5, 2$) are plotted as filled symbols. The points indicate the boundary at which Breslin & Skalak (1959) observed the elimination of ventilated cavities; the specific stage of elimination was not specified in the original report, but is judged from context to be the cessation of FV flow, which has been defined as washout in the present work. Equation (1.2), shown as the black dashed line, represents the lower bound on stable FV flow proposed by Breslin & Skalak (1959).

It should be noted that the boundary given by (1.2) is valid only for $Fn_h \geqslant 3$ (Breslin 1958), above the horizontal line in figure 27. This restricts usage of the boundary to relatively low values of C_L. It should be recalled also that Breslin & Skalak (1959) defined (1.2) such that C_{L_w} is the instantaneous lift coefficient, measured when the hydrofoil is in an FW flow at the conditions under which ventilation elimination occurred. This makes (1.2) difficult to apply directly, because the lift coefficient may be unknown for FW flows at the combination of α and Fn_h observed at the moment of washout. It should be recalled that in figure 15, the approximated intersection points between affine fits through the FV and FW lift coefficients formed a locus of intersection points. In order to justify the application of (1.2) to lift coefficients measured in the FV regime, the orthographic projections of these loci are plotted as bold lines in figure 27, where the lines closely follow the experimentally observed washout boundaries. This means that, at the conditions of washout, the lift coefficients in the FV, PV and FW regimes are approximately equal, so the measured C_L at washout is a suitable approximation of C_{L_w}. As shown in figure 27, equation (1.2) overpredicts the washout Fn_h for a given C_L. In fact, it

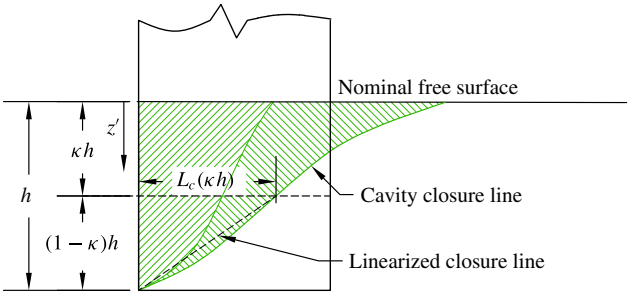

FIGURE 28. (Colour online) Sketch of the cavity topology. The cavity stability criterion of § 3.2 is expressed using a two-point linearization of the cavity closure line. When the slope of the linearized cavity closure line approaches unity ($\bar{\Phi} = 45°$), it is hypothesized that washout is imminent.

passes through only a few of the experimental points from Breslin & Skalak (1959), while washout was never observed at $Fn_h > 3$ in the present experiments.

There are several reasons why the experimentally observed washout boundaries would differ between the present study and that of Breslin & Skalak (1959). The first is the difference in section profiles. As mentioned in § 4.1.3, the present model has a rectangular section aft of mid-chord, while both of the models used by Breslin & Skalak (1959) had sharp trailing edges and convex curvature on the suction surfaces aft of mid-chord. As a result, washout may have occurred at higher Froude numbers for the latter model because the re-entrant jet was enhanced by an adverse pressure gradient developed on the wetted portion of the suction surface. Another factor is the difference in size between the two models. The present model is approximately 4–5 times as large as those used by Breslin & Skalak; the smaller model would be more susceptible to surface-tension effects (Wetzel 1957), where spray sheets close and cut off the supply of air to the cavity in a process called cavity 'choking' (Elata 1967). Equation (1.2) also overpredicts the washout boundary of Breslin & Skalak (1959) for $3 < Fn_h < 6$. This occurs because (1.2) was derived from a linearized fit at very large Fn_h and vanishingly small C_L. Equation (1.2) does form an upper bound on all other presented experimental data, so it is appropriate to consider it as a boundary above which FV flow is likely to be stable, but not a boundary below which full ventilation is necessarily unstable. To develop an improved washout scaling relation, the kinematic stability boundary on the cavity shape ($\bar{\Phi} = 45°$) can be used, along with models for the cavity length (L_c), lift coefficient (C_L), Froude number (Fn_h), aspect ratio (AR_h) and angle of attack (α). An initial attempt was presented by Harwood *et al.* (2014), but an improved scaling approach was deemed necessary.

Figure 28 schematically depicts an FV cavity. A sectional cut is taken at a dimensionless depth of $\kappa = z'/h$ and a linear approximation of the cavity closure angle is made between this section and the immersed tip – a distance of $(1-\kappa)h$. The stability limit of $\bar{\Phi} = 45°$ is equivalent to a unity-slope condition on this linearization. To model the cavity length at the section in question, equation (1.8) is used, giving

$$\frac{L_c(z' = \kappa h)}{c} = (1-\kappa)\frac{h}{c} = 4.62\frac{\alpha_{2D}(z' = \kappa h)}{\sigma_c(z' = \kappa h)}. \tag{4.1}$$

The next step is to infer the sectional lift coefficient at the representative section from the 3D lift coefficient, which requires *a priori* knowledge of the distribution

of lift along the span. A model such as the lifting-line model presented in § 1.2.2 could be used, but an analytical approximation is desirable in this case, in order to derive a closed-form scaling relation. An elliptical shape function may be applied to the lift distribution as a simple approximation for rectangular wings (Glauert 1943), and one that retains the salient features of the lift distribution shown in figure 3. The low aspect ratio is not a concern because the elliptical distribution can be scaled such that integration along the span yields the experimentally measured 3D lift coefficient. Thus, the sectional lift coefficient at the representative section is taken to be

$$C_{l_{2D}}(z' = \kappa h) = \frac{4}{\pi} C_L \sqrt{1 - (2\kappa - 1)^2}. \tag{4.2}$$

The effective angle of attack can be found by substituting $L_c/c = (1-\kappa)AR_h$ into (1.9) to find a_0, giving

$$\begin{aligned}\alpha_{2D}(z' = \kappa h) &= \arcsin\left(\frac{C_{l_{2D}}(z' = \kappa h)}{a_0(z' = \kappa h)}\right) \approx \frac{C_{l_{2D}}(z' = \kappa h)}{a_0(z' = \kappa h)} \\ &= \frac{4C_L\sqrt{\kappa - \kappa^2}\{4\pi[(1-\kappa)AR_h]^3 - 4\pi[(1-\kappa)AR_h]^2 + 3\pi[(1-\kappa)AR_h] + 2\}}{\pi\{\pi^2[(1-\kappa)AR_h]^3 - 4\pi[(1-\kappa)AR_h]^2 + 9\pi(1-\kappa)AR_h + 2\pi\}}.\end{aligned} \tag{4.3}$$

It follows from (1.12) that

$$\sigma_c = \frac{2}{Fn_h^2}\frac{z'}{h} = \frac{2}{Fn_h^2}\kappa, \tag{4.4}$$

which may be substituted into (4.1), along with (4.3). The representative section of the hydrofoil is taken at mid-span ($\kappa = 0.5$), with the reasoning that any re-entrant jet posing a threat of destabilization to the flow is anticipated to be reflected about the deeply submerged portions of the cavity. Solving for Fn_h yields the semi-theoretical washout Froude number,

$$Fn_h = \frac{\pi}{4}\sqrt{\frac{\dfrac{\pi}{2}AR_h^4 - 4AR_h^3 + 18AR_h^2 + 8AR_h}{2.31C_L(\pi AR_h^3 - 2\pi AR_h^2 + 3\pi AR_h + 4)}}. \tag{4.5}$$

The boundaries given by (4.5) are shown in figure 29, again with the data of Breslin & Skalak (1959) and (1.2). The present experimental washout boundary is captured very well by (4.5). The data of Breslin & Skalak (1959) are reasonably well approximated by the present theory for $Fn_h \leqslant 3$, while (1.2) better approximates the points at very small values of C_L and $Fn_h > 3$.

The value of C_L is often not known *a priori*, requiring it to be inferred as well. Again, an approach such as the lifting-line model from § 1.2 may be used to predict C_L for given operating conditions. However, it is more convenient to implement an analytical model of C_L as function of α, AR_h and Fn_h, so that the washout boundary may be represented as a function of α and Fn_h without the necessity of solving (1.19) for each condition. In § 4, it was shown that the instantaneous hydrodynamic load coefficients in unsteady flows did not differ materially from those measured in steady flows. A model that suitably predicts the steady-state lift coefficient at low Fn_h may, as a result, be substituted into the C_L term in (4.5). It should be recalled that (1.20)

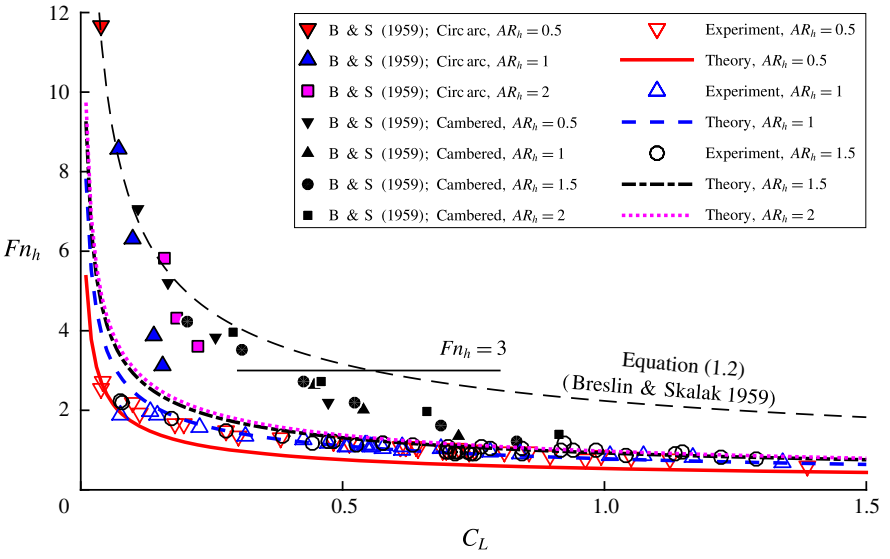

FIGURE 29. (Colour online) Scaled washout boundary in $C_L - Fn_h$ space. Data from the present experiments and from Breslin & Skalak (1959) are plotted. The stability boundary of Breslin & Skalak (1959) (1.2) overpredicts the washout Froude numbers, while the present semi-theoretical boundary (4.5) captures the present experimental data across the range of C_L, and captures the data of Breslin & Skalak (1959) for $C_L \gtrsim 0.6$.

may be used to model C_L by assuming a representative value of a_0. Equation (1.22) can be used again to calculate the lift-weighted mean, a_0^*, but doing so requires that the cavity length and lift distributions are known. The distribution of cavity lengths is constrained by the assumption of $\bar{\Phi} = 45°$ to be

$$\frac{L_c(\kappa)}{c} = AR_h(1-\kappa). \tag{4.6}$$

Equation (4.6) may be substituted into (1.9) to obtain $a_0(\kappa)$. The assumed elliptical lift distribution is scaled to yield an integral of one, giving the shape function,

$$E(\kappa) = \frac{4}{\pi}\sqrt{1-(2\kappa-1)^2}. \tag{4.7}$$

By weighting $a_0(\kappa)$ with $E(\kappa)$, equation (1.22) becomes, under a change of variables,

$$a_0^* = \int_0^1 a_0(\kappa)E(\kappa)\,\mathrm{d}\kappa, \tag{4.8}$$

which is evaluated using numerical integration. The lift-weighted mean value a_0^* is substituted into (1.20), and the predicted C_L is in turn substituted into (4.5). Doing so yields a function of Fn_h, α and AR_h. As before, solving for Fn_h results in a washout Froude number, plotted in figure 30 as a boundary in α–Fn_h space. A value of $\kappa = 0.5$ is again assumed. The boundaries from the present experiments at three aspect ratios ($AR_h = 0.5$, 1, 1.5) are shown as open symbols. Experimental points from Breslin & Skalak (1959) (circular-arc hydrofoil at $AR_h = 0.5$, 1, 1.5 and 2)

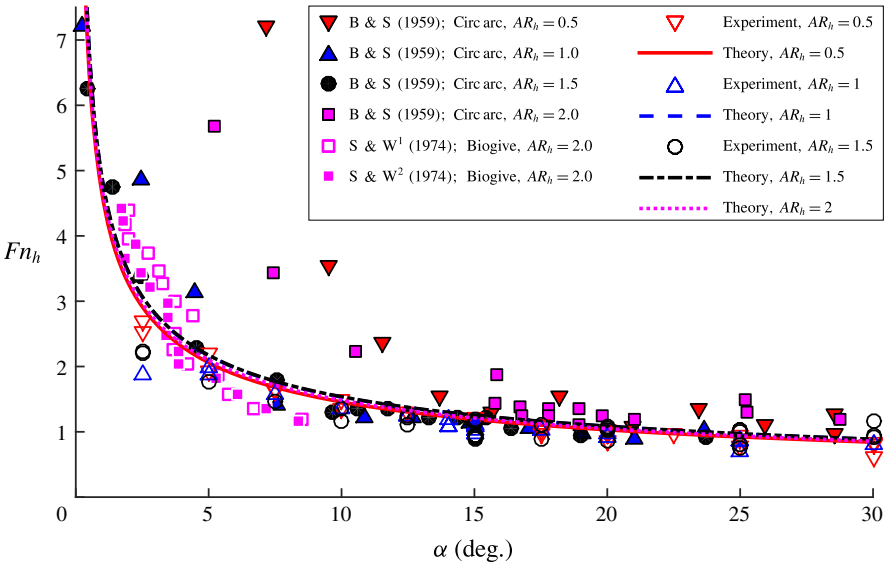

FIGURE 30. (Colour online) Scaled washout boundary in α–Fn_h space. Data from the present experiments and previous experiments are plotted as symbols. B & S, Breslin & Skalak (1959); S & W, Swales *et al.* (1974) experiments in a variable-pressure water tunnel; 1, tests conducted at atmospheric pressure; 2, tests conducted at a reduced pressure of 4.67 kPa.

and Swales *et al.* (1974) (biogival hydrofoil at $AR_h = 2$) are shown for comparison. The two sets of data shown for Swales *et al.* (1974) are from tests conducted in a towing tank at atmospheric pressure and tests in a variable-pressure water tunnel under reduced ambient pressure. The experimental data represent a very diverse range of operating conditions, model sizes and model geometries (see table 1), which are in good general agreement with the semi-theoretical washout boundary.

4.2.2. *Discussion: ventilation elimination*

Ventilation elimination appears to be strongly tied to the potential of the re-entrant jet for destabilization of the flow. The derived scaling relationship approximates the present data much better than does (1.2) for $Fn_h \leqslant 3$. When $Fn_h > 3$, washout appears to occur at vanishingly small angles of attack. The scaling relation is not expected to yield satisfactory results at such small angles of attack because the re-entrant jet may be too thin at such angles to destabilize the cavity (Franc & Michel 2006), as mentioned in § 3.5. Additionally, washout may occur at higher Froude numbers than those predicted by the derived scaling relation for streamlined sections as a result of adverse pressure gradients developed over the afterbody of sections with zero trailing edge thickness. It is also possible that the data from Breslin & Skalak (1959) shown in figures 27 and 29 do not represent washout as it has been defined in this work: if the data denote a stage of elimination other than washout, the scaling approach cannot be expected to adequately capture the respective boundary.

The scaling relationship is based on an assumed elliptical shape function governing the lift distribution. An alternate lift distribution more appropriate to low-aspect-ratio lifting surfaces might yield better results. The use of C_L as an independent variable is useful for cases when instantaneous forces are available. Further modelling of C_L as a function of α is useful for predicting the washout boundary when force measurements

are unavailable, but the attitude of the hydrofoil is known. As shown in figure 29, equation (1.2) overpredicts the washout Froude numbers of the present experiments, while the proposed semi-theoretical washout boundary describes the experimental data of Breslin & Skalak (1959) quite well in α–Fn_h space. Equation (1.2) uses C_{L_w}, or the lift coefficient of wetted flow at the conditions of ventilation washout. Unfortunately, lift in the FW regime may be unknown, and FW flow cannot be sustained for $\alpha > \alpha_s$. Consequently, equation (1.2) is not valid for post-stall angles of attack.

It is also worth noting that the experimental washout boundary of Breslin & Skalak (1959) in figures 27, 29 and 30 deviates from the present semi-theoretical and experimental boundaries quite severely at immersed aspect ratios of $AR_h = 0.5$ and 2.0. This is a result of a distinct bucket shape in the minimum ventilated yaw angle plotted against AR_h in the results from Breslin & Skalak (1959). The reasons for the non-monotonic behaviour are not discussed in the original report, but may be a result of surface-tension effects, given the smaller model scale used.

5. Conclusions

A systematic study has been conducted to examine atmospheric ventilation on a surface-piercing hydrofoil. The authors have endeavoured to standardize disparate terminology used to discuss ventilation and to classify the attending processes. The salient flow features of FW, PV and FV flow regimes were described and illustrated. Consideration of the trajectory of the re-entrant jet led to a stability condition on the cavity topology. The condition requires that the mean angle of the cavity closure line from the horizontal plane does not exceed $\bar{\Phi} = 45°$. By augmenting the flow-regime descriptions in the literature with the new condition, a strengthened set of criteria were defined, under which 3D flows may be unequivocally categorized into the three flow regimes.

The realizable steady-state lift was found to be much lower in the FV regime than in the FW regime. Drag was not strongly affected by ventilation, and the change in yawing moment indicated a progressive movement of the centre of pressure towards mid-chord with the onset of ventilation. The steady-state lift in the FV regime was shown to decrease monotonically with increasing Froude number. These observations were consistent with previous studies. The FW and FV flow regimes overlap one another, constituting a bi-stable range of α, also consistent with past work. The bi-stable range of operating conditions is bounded by the bifurcation boundary and the stall boundary (respective loci of bifurcation angles α_b and stall angles α_s). The experimentally observed flow regimes were mapped as functions of α and Fn_h, revealing three distinct stability regions. Near the boundary between FV and FW flows, the steady lift coefficients are nearly the same in all three steady-state flow regimes.

Ventilation transition mechanisms were classified as ‘formation’ or ‘elimination’ mechanisms for processes that respectively enhance or detract from the size and/or stability of a ventilated cavity. Formation was further decomposed into ‘inception’ and ‘stabilization’ events. Elimination was likewise decomposed into ‘washout’ and ‘rewetting’. The individual stages of formation and elimination separate the three steady-state flow regimes. The transition between stable steady-state flow regimes was shown to occur where stability regions overlapped or abutted one another. Ventilation transition events either occurred spontaneously at the boundary of a stability region or occurred as the result of external perturbation when the flow was in a bi-stable condition.

In the present experiments, ventilation formation was preceded in all cases by leading edge flow separation, indicated by surface-flow visualizations. At sub-stall

angles of attack $\alpha_b \leqslant \alpha < \alpha_s$, ventilation formation occurred when air was introduced from an external source (a high-pressure blower) into a stable separation bubble at the leading edge. Near the stall boundary ($\alpha \approx \alpha_s$) for $AR_h = 1$ only, air entered through the low-pressure core of the tip vortex. At post-stall angles of attack ($\alpha \geqslant \alpha_s$), vortical structures in the eddying stalled wake disrupted the free-surface seal at all immersed aspect ratios, allowing air to enter the large separation bubble. The stall angle α_s was found to be approximately 14°–15° for all Froude numbers at $AR_h = 1$ and $AR_h = 1.5$. Smaller immersed aspect ratios yielded slightly larger values of α_s.

Ventilation washout (the first stage of elimination) occurs when an FV cavity is destabilized by the re-entrant jet at moderate to large α ($\alpha \geqslant 5°$). A destabilizing re-entrant jet develops when the angle of the cavity closure is $\bar{\Phi} \geqslant 45°$, violating the stability condition established for FV flows. At lower angles of attack, other washout mechanisms may be expected to dominate, including choking or gradual turbulent reattachment of the flow, dependent upon the section shape, the scale of the model and the speed. The lower stability boundary for FV flow proposed by Breslin & Skalak (1959) is confined to small values of C_L and large values of Fn_h ($C_L < 0.5$; $Fn_h > 3$). A new scaling relationship was developed that adequately describes the experimentally observed washout boundary from the present experiments across the entire range of C_L, α and Fn_h. The new scaling relation also captures the washout boundaries from experiments by Breslin & Skalak (1959) at moderate to large C_L and α ($C_L \gtrsim 0.5$; $\alpha \gtrsim 5°$) and experiments by Swales *et al.* (1974) across a wide range of α and σ_v.

The lifting-line model presented in this work is intended to qualitatively, rather than quantitatively, describe the effects of the dominant physics. The model yields surprisingly good predictions of the 3D lift and moment coefficients, cavity topologies and re-entrant jet trajectories, considering that the lifting line is classically relegated to very high aspect ratios. However, it is not anticipated that the modelling approaches based on lifting-line and elliptical lift distributions would yield good results for very small aspect ratios ($AR_h < 0.5$). Additionally, it has been found (though not shown) that the lifting-line model only qualitatively describes the behaviour of hydrodynamic forces with respect to varying Fn_h. The results presented in this work are applicable to moderate Froude numbers ($1 \lesssim Fn_h \lesssim 4$), where hydrostatic and dynamic pressures are of the same order of magnitude. In this work, and in the literature, it has been observed that the Froude number ceases to be a dominant parameter for $Fn_h > 4$. At higher speeds, vaporous cavitation may also be a dominant factor, as indicated by Waid (1968) and Rothblum *et al.* (1969).

Acknowledgements

This material is based upon work supported by the National Science Foundation Graduate Student Research Fellowship under grant no. DGE 1256260 and by the Naval Engineering Education Center (Award no. N65540-10-C-003), with support from Dr T. Fu of the Naval Surface Warfare Center, Carderock Division.

Supplementary movies

Supplementary movies are available at http://dx.doi.org/10.1017/jfm.2016.373.

Appendix A. Plots of hydrodynamic load coefficients

In this appendix, the coefficients of lift, drag and moment are illustrated for various values of Fn_h, α and AR_h. The dashed lines indicate affine fits through the mean values. Grey bars indicate the uncertainty (from table 3), and black bars indicate $\pm$ one standard deviation of the respective time series data.

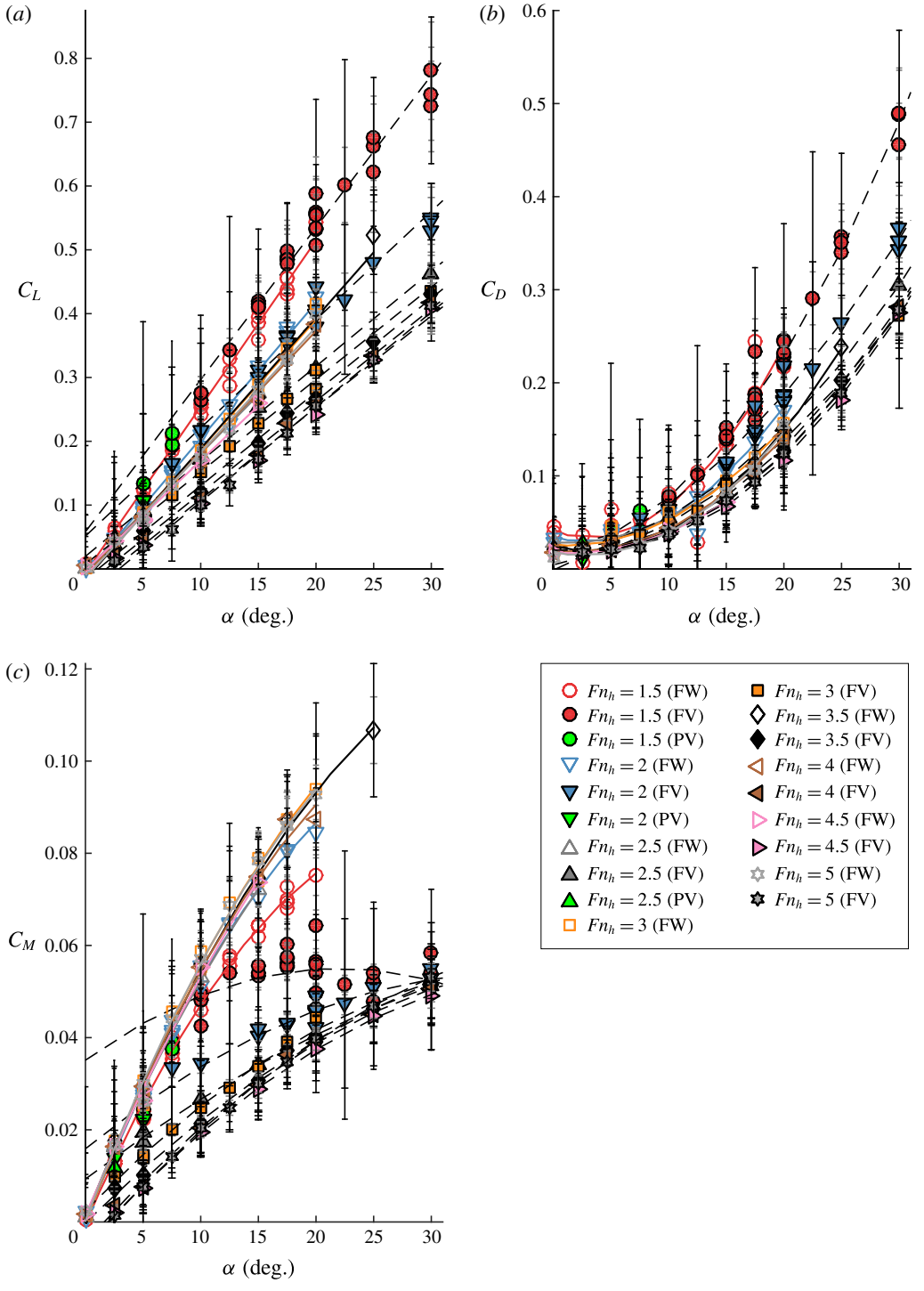

FIGURE 31. (Colour online) Hydrodynamic load coefficients as functions of α and Fn_h for $AR_h = 0.5$.

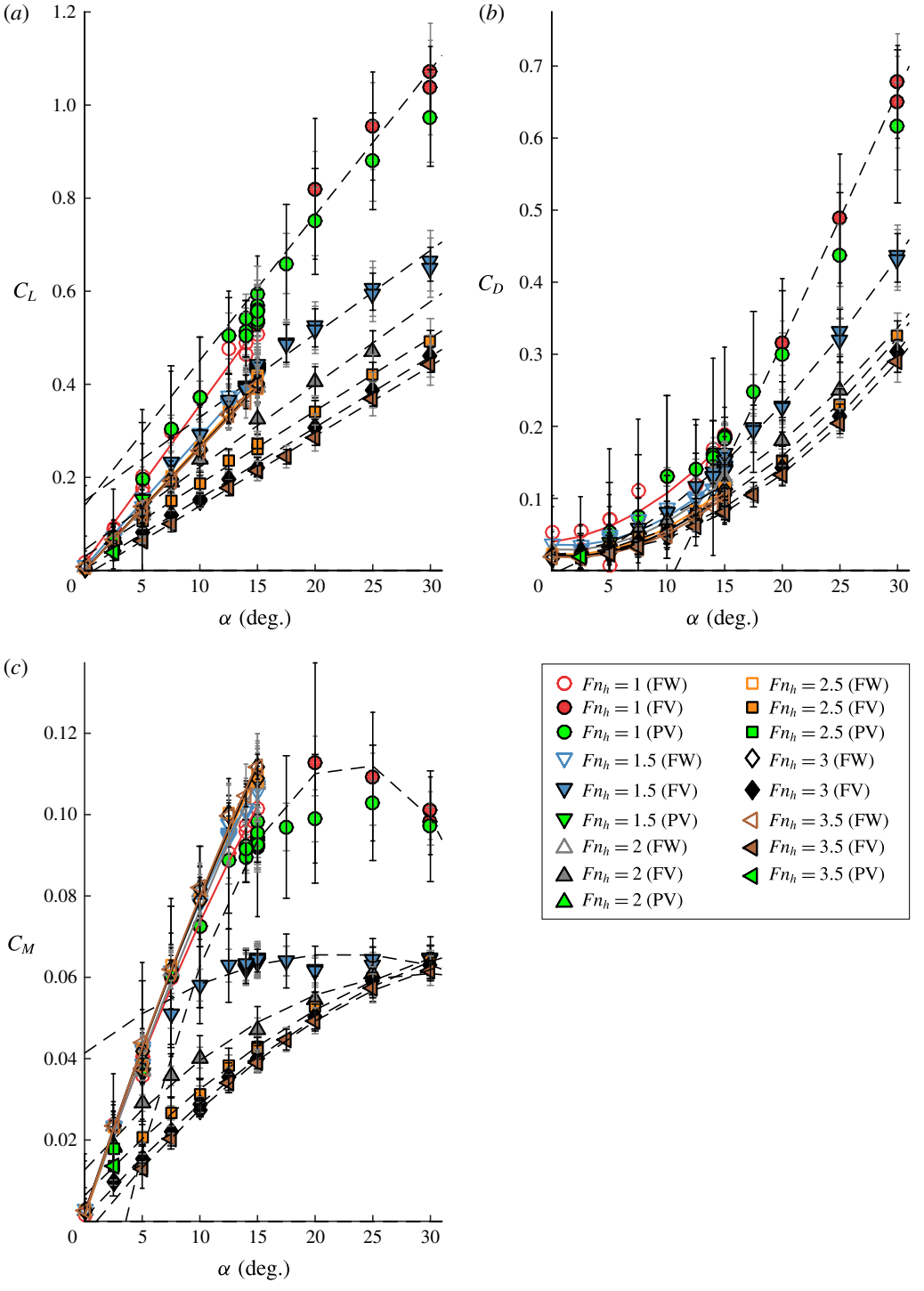

FIGURE 32. (Colour online) Hydrodynamic load coefficients as functions of α and Fn_h for $AR_h = 1$.

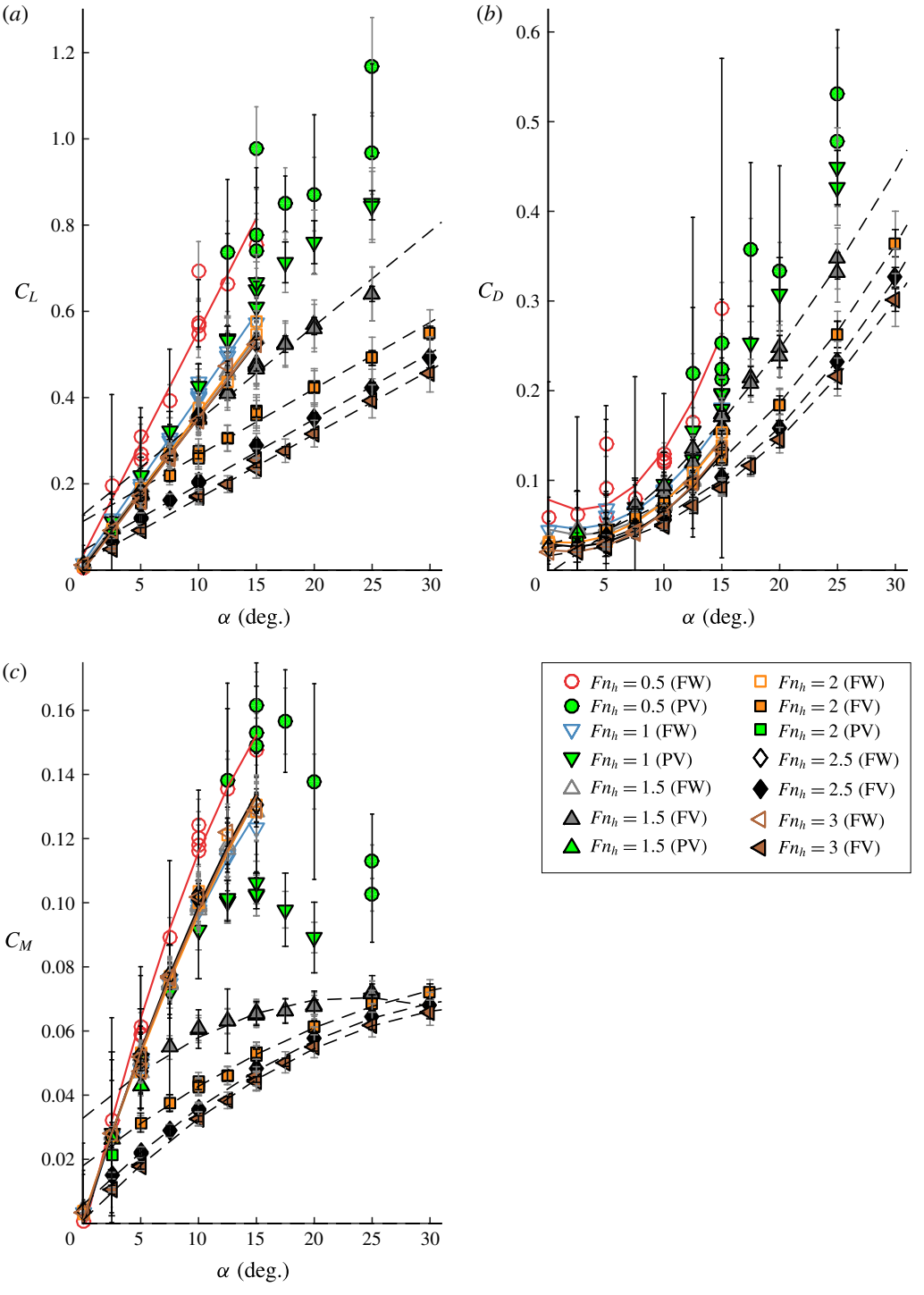

FIGURE 33. (Colour online) Hydrodynamic load coefficients as functions of α and Fn_h for $AR_h = 1.5$.

Appendix B. Order-of-magnitude analysis of added mass

Consider a representative section of the hydrofoil as a 2D flat plate at an angle of attack α, in an infinite domain, with an instantaneous inflow velocity of $u = \dot{X}$, and accelerating at a constant rate of $\ddot{X} = a$. The lift and drag on the plate are

$$\left.\begin{aligned} L &= L_{unsteady} + L_{steady}, \\ D &= D_{unsteady} + D_{steady}. \end{aligned}\right\} \tag{B 1}$$

The unsteady forces are limited to the inertial influence of the fluid as the body accelerates. Potential flow gives the inertial component in the Y direction due to accelerations in X as

$$\begin{aligned} L_{unsteady} &= m_{21}\ddot{X} \\ &= \frac{1}{2}\pi\rho\left(\frac{c}{2}\right)^2 \sin(2\alpha)\ddot{X}. \end{aligned} \tag{B 2}$$

The inertial component in the X direction is

$$\begin{aligned} D_{unsteady} &= m_{11}\ddot{X} \\ &= \pi\rho\left(\frac{c}{2}\right)^2 \sin^2(\alpha)\ddot{X}, \end{aligned} \tag{B 3}$$

where m_{21} and m_{11} are components of the added-mass tensor $\boldsymbol{m}$. Equation (B 1) becomes

$$\left.\begin{aligned} L &= \frac{\pi}{2}\rho\left(\frac{c}{2}\right)^2 \sin(2\alpha)\ddot{X} + C_L\frac{1}{2}\rho\dot{X}^2 c, \\ D &= \pi\rho\left(\frac{c}{2}\right)^2 \sin^2(\alpha)\ddot{X} + C_D\frac{1}{2}\rho\dot{X}^2 c. \end{aligned}\right\} \tag{B 4}$$

Given that $Fn_h = \dot{X}/\sqrt{gh}$, the ratio of unsteady to steady lift can be expressed as

$$R_L = \frac{L_{unsteady}}{L_{steady}} = \frac{\pi}{4AR_h}\frac{\sin(2\alpha)}{C_L}\frac{\ddot{X}}{g}\frac{1}{Fn_h^2}. \tag{B 5}$$

The ratio of unsteady to steady drag is written as

$$R_D = \frac{D_{unsteady}}{D_{steady}} = \frac{\pi}{2AR_h}\frac{\sin^2(\alpha)}{C_D}\frac{\ddot{X}}{g}\frac{1}{Fn_h^2}. \tag{B 6}$$

The quantities of (B 5) and (B 6) are estimated by order of magnitude as follows:

(1) $\sin^2(\alpha) = O(10^{-1})$ for $\alpha < 30°$;
(2) $\sin(2\alpha) = O(1)$ for $\alpha < 30°$;
(3) $\ddot{X}/g = O(10^{-2})$, assuming $\ddot{X} = a \approx O(1)$ ft s^{-2};
(4) $AR_h = O(1)$;
(5) $C_L = O(1)$;
(6) $C_D = O(10^{-1})$.

The resulting ratios become, after simplification,

$$R_L \approx \frac{\pi}{4} \times 10^{-2}\frac{1}{Fn_h^2} = O\left(\frac{1}{Fn_h^2} \times 10^{-2}\right), \tag{B 7}$$

$$R_D \approx \frac{\pi}{2} \times 10^{-2}\frac{1}{Fn_h^2} = O\left(\frac{1}{Fn_h^2} \times 10^{-2}\right). \tag{B 8}$$

This result suggests that for $Fn_h \ll 1$ only, the inertial forces are of the same order as the steady lift and drag. The relative magnitude of the inertial components vanishes quickly as the speed, and Fn_h, increase, and may be neglected for $Fn_h > 1$.

REFERENCES

ACOSTA, A. J. 1955 Note on partial cavitation of flat plate hydrofoils. *Tech. Rep.* E-19.9. California Institute of Technology.

ACOSTA, A. J. 1973 Hydrofoils and hydrofoil craft. *Annu. Rev. Fluid Mech.* **5** (1), 161–184.

AKCABAY, D. T. & YOUNG, Y. L. 2014 Influence of cavitation on the hydroelastic stability of hydrofoils. *J. Fluids Struct.* **49** (0), 170–185.

BRENNEN, C. E. 1995 *Cavitation and Bubble Dynamics*. Oxford University Press.

BRESLIN, J. P. 1958 Discussion of paper by K. L. Wadlin. In *Proceedings of the Second Symposium on Naval Hydrodynamics*, vol. 1, pp. 434–440. US Office of Naval Research.

BRESLIN, J. P. & SKALAK, R. 1959 Exploratory study of ventilated flows about yawed surface-piercing struts. *Tech. Rep.* 2-23-59W. NASA Tech. Mem., Washington, DC, USA.

CALLENAERE, M., FRANC, J.-P., MICHAEL, J.-M. & RIONDET, M. 2001 The cavitation instability induced by the development of a re-entrant jet. *J. Fluid Mech.* **444**, 223–255.

CHANG, P. K. 1960 Laminar separation of flow around symmetrical struts at zero angle of attack. *J. Franklin Inst.* **270** (5), 382–396.

CHANG, P. K. 1961 Separation of flow. *J. Franklin Inst.* **272** (6), 433–448.

COFFEE, C. W. JR. & MCKANN, R. E. 1953 Hydrodynamic drag of 12- and 21-percent-thick surface-piercing struts. *Tech. Rep.* 3093. NACA Tech. Note, Washington, DC, US.

DE LANGE, D. F. & DE BRUIN, G. J. 1998 Sheet cavitation and cloud cavitation, re-entrant jet and three-dimensionality. In *Fascination of Fluid Dynamics*, pp. 91–114. Springer.

ELATA, C. 1967 Choking of strut-ventilated foil cavities. *Tech. Rep.* 605-2. Hydronautics, Inc.

EMMONS, H. W., CHANG, C. T. & WATSON, B. C. 1960 Taylor instability of finite surface waves. *J. Fluid Mech.* **7**, 177–193.

FALTINSEN, O. M. 2005 *Hydrodynamics of High-Speed Marine Vehicles*. Cambridge University Press.

FRANC, J. P. & MICHEL, J. M. 2006 *Fundamentals of Cavitation*. Springer.

GAULT, D. A. 1957 A correlation of low-speed, airfoil-section stalling characteristics with Reynolds number and airfoil geometry. *Tech. Rep.* 3963. NACA Tech. Note.

GLAUERT, H. 1943 *The Elements of Aerofoil and Airscrew Theory*. Cambridge University Press.

GREEN, S. 1988 Tip vortices – single phase and cavitating flow phenomena. PhD thesis, California Institute of Technology.

GREEN, S. I. & ACOSTA, A. J. 1991 Unsteady flow in trailing vortices. *J. Fluid Mech.* **227**, 107–134.

HARWOOD, C. M., BRUCKER, K. A., MIGUEL, F., YOUNG, Y. L. & CECCIO, S. L. 2014 Experimental and numerical investigation of ventilation inception and washout mechanisms of a surface-piercing hydrofoil. In *Proceedings of the 30th Symposium on Naval Hydrodynamics, Hobart, Tasmania*.

HARWOOD, C. M. & YOUNG, Y. L. 2014 A physics-based gap-flow model for potential flow solvers. *J. Ocean Engng* **88**, 578–587.

HECKER, R. & OBER, G. 1974 Flow separation, reattachment, and ventilation of foils with sharp leading edge at low Reynolds number. *Tech. Rep.* AD-787500. Naval Ship Research and Development Center, USA.

HELMBOLD, H. B. 1942 Der unverwundene Ellipsenflugel als tragende Flanche. In *Jahrbuch 1942 der Deutsch Luftfahrtforsch*, pp. I111–I113. R. Oldenberg.

KICENIUK, T. 1954 A preliminary experimental study of vertical hydrofoils of low aspect ratio piercing a water surface. *Tech. Rep.* E-55.2. California Instute of Technology.

LABERTEAUX, K. R. & CECCIO, S. L. 2001*a* Partial cavity flows. Part 1. Cavities forming on models without spanwise variation. *J. Fluid Mech.* **431**, 1–41.

LABERTEAUX, K. R. & CECCIO, S. L. 2001*b* Partial cavity flows. Part 2. Cavities forming on test objects with spanwise variation. *J. Fluid Mech.* **431**, 43–63.

LARSSON, L. & RAVEN, H. C. 2010 *Principles of Naval Architecture Series – Ship Resistance and Flow* (ed. J. R. Paulling). Society of Naval Architects and Marine Engineers (SNAME).

PERRY, B. 1955 Experiments on struts piercing the water surface. *Tech. Rep.* E-55.1. California Instute of Technology, Pasadena.

POGOZELSKI, E. M., KATZ, J. & HUANG, T. T. 1997 The flow structure around a surface piercing strut. *Phys. Fluids* **9** (5), 1387–1399.

ROTHBLUM, R. S. 1977 Investigation of methods of delaying or controlling ventilation on surface-piercing struts. PhD thesis, University of Leeds.

ROTHBLUM, R. S., MAYER, D. A. & WILBURN, G. M. 1969 Ventilation, cavitation and other characteristics of high speed surface-piercing strut. *Tech. Rep.* 3023. Naval Ship Research and Development Center, Washington DC.

ROTHBLUM, R. S., MCGREGOR, R. C. & SWALES, P. D. 1974 Effect of roughness, wettability and speed on the ventilation characteristics of surface piercing hydrofoil struts. In *Proceedings of the International Hovering Craft, Hydrofoil, and Advanced Transit Systems Conf.*, pp. 235–243.

SWALES, P. D., WRIGHT, A. J., MCGREGOR, R. C. & COLE, B. N. 1973 Pressure, flow visualisation and ventilation. *Hovering Craft Hydrofoil* **13** (1), 11–16.

SWALES, P. D., WRIGHT, A. J., MCGREGOR, R. C. & ROTHBLUM, R. 1974 Mechanism of ventilation inception on surface piercing foils. *J. Mech. Engng Sci.* **16** (1), 18–24.

TASSIN-LEGER, A. & CECCIO, S. L. 1998 Examination of the flow near the leading edge of attached cavitation. Part 1. Detachment of two-dimensional and axisymmetric cavities. *J. Fluid Mech.* **376**, 61–90.

TAYLOR, G. 1950 The instability of liquid surfaces when accelerated in a direction perpendicular to their planes I. *Proc. R. Soc. Lond.* A **201**, 192–196.

TULIN, H. P. 1953 Steady two-dimensional cavity flows about slender bodies. *Tech. Rep.* 834. United States Navy Department – David W. Taylor Model Basin, Bethesda.

WADLIN, K. L. 1958 Mechanics of ventilation inception. In *Proceedings of the Second Symposium on Naval Hydrodynamics*, vol. 1, pp. 425–445. US Office of Naval Research.

WAID, R. L. 1968 Experimental investigation of the ventilation of vertical surface-piercing struts in the presence of cavitation. *Tech. Rep.* AD0738493. Naval Ship Research and Development Center.

WETZEL, J. M. 1957 Experimental studies of air ventilation of vertical, semi-submerged bodies. *Tech. Rep.* 57. St. Anthony Falls Hydraulic Laboratory, University of Minnesota.

YOUNG, Y. L. & BRIZZOLARA, S. 2013 Numerical and physical investigation of a surface-piercing hydrofoil. In *Proceedings of the Third International Symposium on Marine Propulsors SMP, Launceston* (ed. J. Binns, R. Brown & N. Bose), pp. 1–8. Australian Maritime College, University of Tasmania.